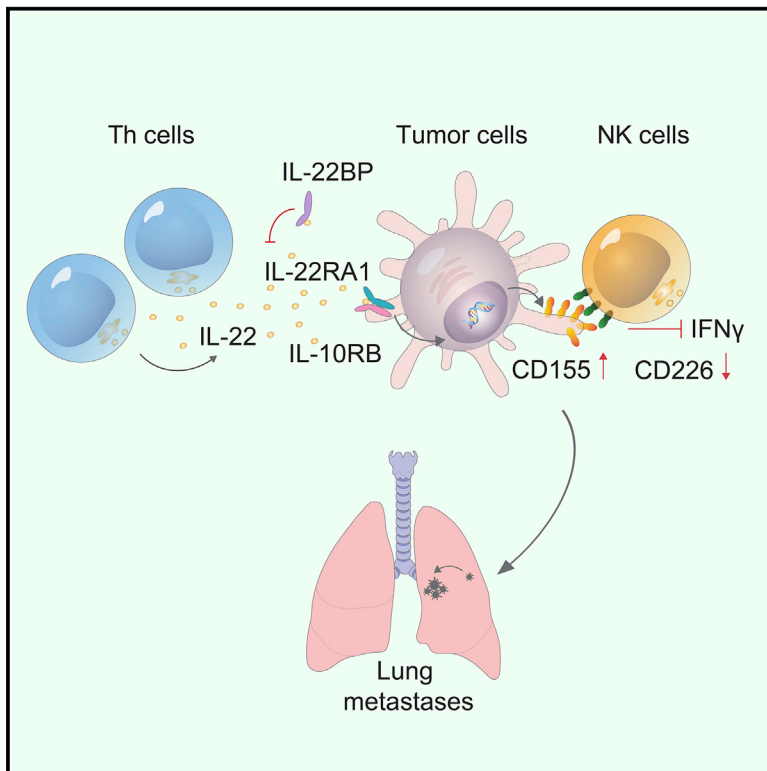# Immunity

T cell-derived interleukin-22 drives the expression of CD155 by cancer cells to suppress NK cell function and promote metastasis

Graphical abstract

Authors

Daria Briukhovetska,
Javier Suarez-Gosalvez,
Cornelia Voigt, ..., Samuel Huber,
Stefan Endres, Sebastian Kobold

Correspondence

sebastian.kobold@
med.uni-muenchen.de

In brief

Metastatic disease is the terminal and most lethal stage of cancer. Briukhovetska et al. find that interleukin-22 produced by Th cells increases the expression of CD155 in cancer cells, which in turn abrogates NK cell function by promoting the internalization of the activating receptor CD226. This axis promotes an immunosuppressive niche that enables lung metastases.

Highlights

- IL-22 from Th cells acts on IL-22RA1^{+} tumor cells to promote lung metastases

- Mechanistically, IL-22 induces overexpression of CD155 on tumor cells

- Excessive CD155 promotes internalization of CD226 in NK cells, rendering them inert

- IL-22-CD155 signature governs early-stage lung and breast cancer patients' survival

CellPress

Article

T cell-derived interleukin-22 drives the expression of CD155 by cancer cells to suppress NK cell function and promote metastasis

Daria Briukhovetska,[1,13] Javier Suarez-Gosalvez,[1,13] Cornelia Voigt,[1,13] Anamarija Markota,[1] Anastasios D. Giannou,[2,3] Maryam Schübel,[1] Jakob Jobst,[1] Tao Zhang,[2] Janina Dörr,[1] Florian Märkl,[1] Lina Majed,[1] Philipp Jie Müller,[1] Peter May,[1] Adrian Gottschlich,[1] Nicholas Tokarew,[1] Jöran Lücke,[2,3] Arman Oner,[1] Melanie Schwerdtfeger,[1] David Andreu-Sanz,[1] Ruth Grünmeier,[1] Matthias Seifert,[1] Stefanos Michaelides,[1] Michael Hristov,[4] Lars M. König,[1] Bruno Loureiro Cadilha,[1] Oleg Mikhaylov,[5] Hans-Joachim Anders,[6] Simon Rothenfusser,[1,7] Richard A. Flavell,[8,9] Daniela Cerezo-Wallis,[10] Cristina Tejedo,[10] María S. Soengas,[10] Tobias Bald,[11] Samuel Huber,[2] Stefan Endres,[1,7,12] and Sebastian Kobold[1,7,12,14,*]

[1]Division of Clinical Pharmacology, Klinikum der Universität München, 80337 Munich, Germany
[2]Section of Molecular Immunology and Gastroenterology, I. Department of Medicine, and Hamburg Center for Translational Immunology (HCTI), University Medical Center Hamburg-Eppendorf, 20246 Hamburg, Germany
[3]Department of General, Visceral and Thoracic Surgery, University Medical Center Hamburg-Eppendorf, 20246 Hamburg, Germany
[4]Institute for Cardiovascular Prevention (IPEK), University Hospital, Klinikum der Universität München, Munich, Germany
[5]TwentyBN, 10245 Berlin, Germany
[6]Division of Nephrology, Department of Medicine IV, Klinikum der Universität München, 80337 Munich, Germany
[7]Einheit für Klinische Pharmakologie (EKLiP), Helmholtz Zentrum München, German Research Center for Environmental Health (HMGU), 85764 Neuherberg, Germany
[8]Department of Immunobiology, School of Medicine, Yale University, New Haven, CT 06520, USA
[9]Howard Hughes Medical Institute, Yale University School of Medicine, New Haven, CT 06520, USA
[10]Melanoma Laboratory, Molecular Oncology Program, Spanish National Cancer Research Centre (CNIO), 28029 Madrid, Spain
[11]Institute of Experimental Oncology, Medical Faculty, University Hospital Bonn, University of Bonn, 53127 Bonn, Germany
[12]Center for Translational Cancer Research (DKTK), Partner Site Munich, 80336 Munich, Germany
[13]These authors contributed equally
[14]Lead contact
*Correspondence: sebastian.kobold@med.uni-muenchen.de
https://doi.org/10.1016/j.immuni.2022.12.010

SUMMARY

Although T cells can exert potent anti-tumor immunity, a subset of T helper (Th) cells producing interleukin-22 (IL-22) in breast and lung tumors is linked to dismal patient outcome. Here, we examined the mechanisms whereby these T cells contribute to disease. In murine models of lung and breast cancer, constitutional and T cell-specific deletion of *Il22* reduced metastases without affecting primary tumor growth. Deletion of the IL-22 receptor on cancer cells decreases metastasis to a degree similar to that seen in IL-22-deficient mice. IL-22 induced high expression of CD155, which bound to the activating receptor CD226 on NK cells. Excessive activation led to decreased amounts of CD226 and functionally impaired NK cells, which elevated the metastatic burden. IL-22 signaling was also associated with CD155 expression in human datasets and with poor patient outcomes. Taken together, our findings reveal an immunosuppressive circuit activated by T cell-derived IL-22 that promotes lung metastasis.

INTRODUCTION

The major hallmark of neoplastic progression and the primary cause of cancer-related mortality is the ability of cancer cells to disseminate to secondary sites and form metastases.[1,2] The formation of metastasis can be prevented by immunosurveillance involving natural killer (NK), cytotoxic, and T helper (Th) 1 cells.[3,4] In contrast, regulatory T cells (Treg), circulating monocytes, and Th cell-derived IL-17A form an immunosuppressive microenvironment, enabling immune escape and promoting metastases.[4–6] Therefore, it is critical to identify signaling cascades that define the function of pro- vs. anti-tumorigenic immune cells.[7,8]

Interleukin-22 (IL-22) is a cytokine produced by Th17 and, in humans, also by the Th1 subset, known to promote cancer cell growth, enhance migration, protect from apoptosis, induce epithelial-to-mesenchymal transition, and sustain stemness of malignant cells.[9–13] It also promotes early carcinogenesis, acting on precursor lesions or immature cancer stem cells.[14–18] IL-22-producing cells, mainly Th cells, but also gamma delta (γδ) T cells, invariant natural killer T (iNKT) cells, and innate lymphoid cells (ILCs), have been detected in primary cancer lesions.[19–24]

IL-22 is expressed at biologically relevant levels in breast, colon, lung, gastric, and hepatocellular carcinoma.[9,11,12,25,26] In most studies, its expression is associated with a poor prognosis, higher disease stage, and faster tumor progression.[13,22–24,27–29] IL-22 acts exclusively through the IL-22 receptor (IL-22R) comprised of two subunits, IL-22RA1 and IL-10RB.[30,31] The action of secreted IL-22 is modulated by an inhibitor, the IL-22 binding protein (IL-22BP, IL-22RA2), a homolog of IL-22RA1, that is mainly produced by myeloid cells.[32,33] Under steady-state conditions, IL-22 is an essential homeostatic cytokine at epithelial barriers such as the gut, lung, and skin.[34,35] At these sites, IL-22 promotes protection, regeneration, and repair to sustain barrier integrity,[36,37] and its absence exacerbates inflammation-induced carcinogenesis.[13,38] Together, these data highlight the broad, context-dependent functions of IL-22 in both physiological and pathological conditions.

Upon receptor binding, IL-22 triggers the Janus kinases Jak1 and Tyk2 to phosphorylate STAT3, STAT1, or STAT5, but IL-22 can initiate other downstream pathways, including the mitogen-activated protein kinases (MAPK) cascade or PI3K-Akt-mTOR signaling, depending on the cellular context.[13,36,39–44] This diversity of signaling pathways is reflected by the multitude of physiological effects that have been associated with IL-22 signaling, including those described above, as well as protection from genotoxic damage and the induction of anti-bacterial peptides, mucus, pro- and anti-inflammatory cytokines, and chemokines.[36,38,39,45,46]

Cancer cells induce the production of IL-22 from Th cells in breast and lung cancer patients.[12,47,48] NLRP3 inflammasome-driven release of IL-1β induces IL-22 production from T cells in the tumor, and both IL-22+ Th cells and an NLRP3-IL-1β signature can be found in tumor samples of breast and lung cancer.[48,49] Here, we set out to delineate a mechanism whereby IL-22 promotes breast and lung cancer progression. We found that IL-22 promotes metastasis spread to the lung, revealing a circuit wherein IL-22 mediated immunosuppression in the metastatic niche by promoting the expression of CD155 on cancer cells, which was associated with decreased expression of CD226 on NK cells and reduced interferon-γ (IFNγ) production. Clinical data indicate that activation of such pathways is linked to patient outcomes.

RESULTS

IL-22 impacts disseminated cancer cells in syngeneic mouse models of lung and breast carcinoma

To understand the impact of the IL-22-IL-22R1 signaling axis on cancer progression, we analyzed syngeneic murine models of breast and lung carcinoma. As cancer patients mostly succumb to metastatic disease, we recapitulated this with phenotypically relevant models. We implanted either 4T1 breast cancer or Line-1 lung cancer cells subcutaneously (s.c.) in the right flank of wild-type mice (WT) and mice lacking IL-22 expression ($Il22^{-/-}$) (Figure 1A). IL-22 did not impact the outgrowth of the primary tumors in either model (Figures 1B and 1C). Upon reaching pre-defined termination criteria (tumor >225mm² or ulceration), the lungs were the main metastatic site in our model with occasional metastases found elsewhere (not shown). $Il22^{-/-}$ mice demonstrated decreased metastatic dissemination of

Line-1 and 4T1 cells to the lung compared with wild-type animals independently of the primary tumor size using different methods of metastasis detection (Figures 1B, 1C, and S1A). We have also observed a similar metastatic phenotype in an orthotopic model of breast cancer, where 4T1 cells were implanted into the mammary fat pad (Figure S2B). All used methods of blinded macroscopic counting, clonogenic assays, or histology showed high consistency in detecting lower metastatic burden in $Il22^{-/-}$ animals (Figures 1B, 1C, and S1C). This implicates the pivotal role of IL-22 in the metastatic process.

Next, we forced metastasis through intravenous cancer cell injection, which bypasses the need for tissue detachment and invasion (Figure 1D). Intravenous (i.v.) injections of both cell lines mirrored the phenotype in the subcutaneous model. We could indeed confirm a lower metastatic load in $Il22^{-/-}$ mice (Figures 1E and 1F). These results indicate a specific role for IL-22 in disseminated cells in circulation.

To discern strain-specific effects, we used an E0771 breast cancer model (Figure 1G).[50,51] Intravenous injection of E0771-GFP cells revealed a diminished metastatic burden in $Il22^{-/-}$ animals validated by flow cytometry (Figures 1H and S1D). Similarly, we observed a lower metastatic burden in the liver of mice when E0771-GFP cells were injected intrasplenically (Figure S1E). The entire left lung of E0771-GFP-injected mice was optically cleared following an iDISCO protocol to quantify metastases with light-sheet microscopy in situ (Figure 1I).[52] Here, $Il22^{-/-}$ mice exhibited a reduced propensity to develop metastases, whereas the size of the visualized metastases did not differ and had no specific pattern of their localization (Figure 1J). In summary, IL-22 acted on disseminated cancer cells, enabling breast and lung cancer metastases to the lung.

T cells are the relevant source of IL-22 in the metastatic niche in the lung

We previously identified CD4+ T cells as the main source of IL-22 in primary human lung tumors and bronchoalveolar lavage samples.[12,47,48] To delineate the source of IL-22 in the lungs of our models, we intravenously injected E0771 cells into $Foxp3^{mRFP}$ $Il17a^{GFP}Il22^{sgBFP}$ reporter animals and quantified IL-22+ cells using flow cytometry (Figures 2A and S2A).[53] Populations were defined as CD4+, CD8+ and double-negative (DN) (CD4−, CD8−) αβ T cells (CD3+γδTCR−NK1.1−), γδ T cells (CD3+ γδTCR+NK1.1−), and CD3+NK1.1+ and CD3−NK1.1+ cells (Figures 2B and S2B). We observed an increase in the fraction of CD4+, CD8+ T cells, and NK1.1+ cells that produced IL-22 in the lungs of tumor-injected animals (Figures 2C, S2C, and S2D). Here, CD4+ and CD8+ T cells constituted the majority of IL-22-producing cells in tumor-bearing mice (Figure 2C). Moreover, we identified that such CD4+ T cells produced IL-22 but not IL-17A (Figure 2D). These cells had low CD44 expression, confirming their memory phenotype in line with our previous observations (Figure S2E).[48] To further explore these findings across models, we used intracellular staining to assess the production of IL-22 in the Line-1 s.c. model, which yielded similar results except for a diminished fraction of CD8+ T cell IL-22 producers (Figures S2F–S2I). We could also identify that IL-22+ cells did not co-express IFNγ, which sets apart mouse IL-22 producers from the Th1 subset (Figure 2G).[49] Furthermore, we used confocal microscopy on precision-cut lung slices from reporter
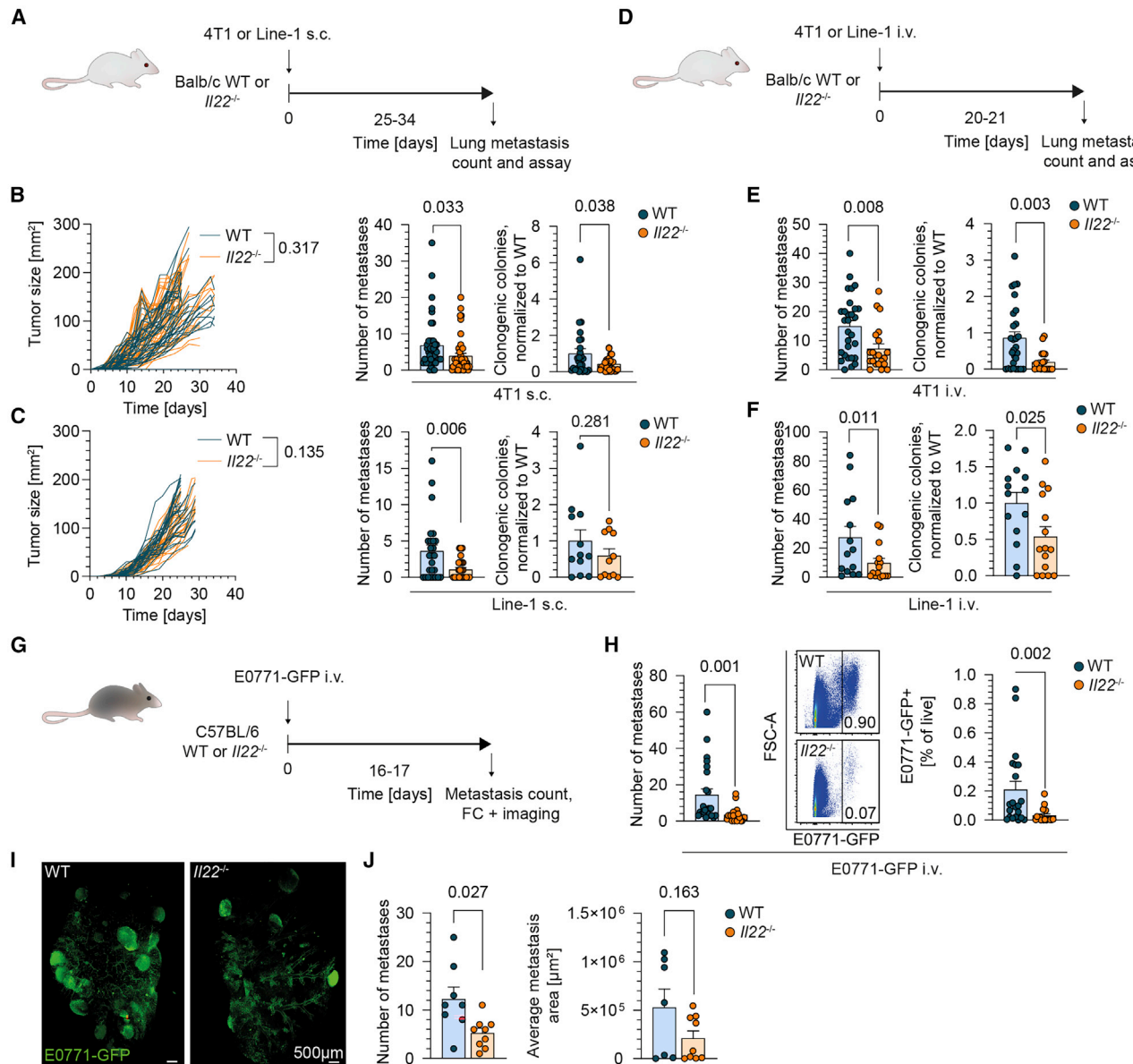
Figure 1. IL-22-knockout reduces the number of lung metastases but does not affect tumor growth in syngeneic mouse models of lung and breast carcinoma

(A) Subcutaneous (s.c.) mouse models of 4T1 breast and Line-1 lung metastasis in wild-type (WT) and $Il22^{-/-}$ animals.

(B and C) Subcutaneous tumor growth, macroscopic metastases in the lungs, and colonies in clonogenic metastasis assay of (B) 4T1 (n = 47 and 48 for tumor growth and metastasis number; n = 27 and 28 for clonogenic assay) (data of six experiments for tumor growth and four independent experiments for metastasis assay in each cell line were pooled) and (C) Line-1 cells (n = 26 and 25 for tumor growth and metastasis number; n = 12 and 11 for clonogenic assay) (data of four experiments for tumor growth and two experiments for metastasis assay were pooled).

(D) Intravenous (i.v.) models of lung cancer metastasis.

(E and F) Numbers of macroscopic metastases in the lungs and colonies in metastasis assay of (E) 4T1 (n = 24 and 29) and (F) Line-1 cells (n = 14 and 15). Data from six experiments for 4T1 and three for Line-1 were pooled. p values are calculated by the mixed-effect two-way analysis for tumor growth and by the Mann-Whitney U test for the number of metastases and clonogenic assay.

(G) Intravenous model of E0771-GFP breast cancer metastasis.

(H) Number of metastases in the lungs (n = 22 and 23). Representative flow cytometry plots of the lung cells. The numbers are the frequency of the parent gate. Frequency of E0771-GFP+ cells among live cells (n = 19 and 21). Data from four experiments were pooled. p values are calculated by the Mann-Whitney U test.

(I) Representative reconstructed 3D images of the left lung from E0771-GFP-injected mice cleared using iDISCO protocol and imaged using light-sheet microscopy. The GFP signal is in green.

(J) Numbers per left lung and the average surface area of metastases (μm^2) per mouse (n = 8 and 9). Data from two experiments were pooled. p values are calculated by Welch's t test. All data are presented as mean ± SEM; p values <0.05 are considered significant. See also Figure S1.

(legend on next page)

animals to interrogate their spatial distribution in the lung of tumor-injected mice. Here, we could identify that such IL-22 and IL-17A producers localize almost exclusively to the metastatic foci (Figure 2E). As demonstrated by flow cytometry, we found no correlation between IL-22 and IL-17A production from the reporter cells in the metastatic foci, indicating that IL-22 and IL-17 are indeed produced by two different cellular subsets. We also confirmed that a large portion of IL-22-producing cells are CD4^{+} T cells (Figure 2E).

As these data indicated a predominant role for T cells in IL-22 production, we generated an $Il22^{flox}Cd4^{cre}$ mouse with a conditional deletion of $Il22$ in all mature T cells (Figure 2F). When challenged with E0771-GFP cells, $Il22^{flox}Cd4^{cre}$ mice had a reduced propensity to develop metastases in the lung, reminiscent of the phenotype observed in the global $Il22^{-/-}$ animals (Figure 2F). However, we could also confirm that cre-recombinase under the control of CD4 promotor completely abolished IL-22 production not only in CD4^{+}, but also in CD8^{+} T cells isolated from the spleen of $Il22^{flox}Cd4^{cre}$ mice, and therefore this model could not be utilized to pinpoint a specific source of IL-22 (Figure S2J). To confirm the role of Th cells as the crucial source of IL-22 in our model, we transferred wild-type and $Il22^{-/-}$ CD4^{+} T cells into $Rag1^{-/-}Il22^{-/-}$ animals that subsequently received E0771-GFP cells i.v. (Figure 2G). Here, we could confirm that IL-22 production by adoptively transferred CD4^{+} T cells is sufficient to promote lung metastases in our model but abolished when using CD4^{+} T cells isolated from $Il22^{-/-}$ animals (Figure 2G). Importantly, differences in metastasis were affected by T cell engraftment upon transfer (Figure S2K). In conclusion, we identified Th cells as a sufficient source of IL-22 that drives metastases in the lung of tumor-bearing mice, and we next sought to identify the relevant target cell.

The expression of IL-22RA1 on tumor cells is indispensable for the formation of metastasis

IL-22RA1 expression is restricted to non-hematopoietic cells and serves as a limiting factor for IL-22 signaling. To interrogate its influence on the metastatic phenotype, we generated a stable $Il22ra1$ deletion in 4T1 and Line-1 cells (Figure 3A). In line with our previous findings, tumor growth of 4T1 $Il22ra1^-$ cells was largely unaffected compared with 4T1 control cells (Figure 3B).

However, mice that were injected with 4T1 $Il22ra1^-$ cells s.c. or i.v. had fewer macroscopic and clonogenic metastases in the lung compared with control 4T1 cells (Figures 3B and 3C). To confirm that this effect is not clone dependent, we generated and analyzed three Line-1 $Il22ra1^-$ clones and tested them against three control clones, which yielded similar results (Figures 3D and 3E). This confirms that IL-22RA1-expressing cancer cells are the relevant target of IL-22 in driving lung metastases.

To rule out the off-target effects of the methodology, we used IL-22BP to inhibit IL-22 signaling. We established 4T1 and Line-1 cell lines that constitutively secreted IL-22BP ($Il22ra2^+$) (Figure S3A). When injected s.c., Line-1 $Il22ra2^+$ cells grew comparably with the control at the implantation site, as previously seen in the $Il22ra1^-$ models and the $Il22^{-/-}$ mice, although 4T1 $Il22ra2^+$ cells grew slower (Figure S3B). Here, 4T1 $Il22ra2^+$ cells had a largely reduced number of metastases when injected s.c. (Figure S3B and S3C). Despite greater variability, the Line-1 $Il22ra2^+$ cells did also form fewer metastases when injected s.c. or i.v. (Figure S3D and S3E). Thus, IL-22 neutralization through IL-22BP largely mimicked the phenotype observed with $Il22ra1^-$ cells and $Il22^{-/-}$ mice, corroborating the relevance of the cytokine for the metastatic process.

IL-22 controls the outgrowth of tumor cells during the early stage of metastatic engraftment

To determine the role of IL-22 signaling during the dissemination process, we analyzed the kinetics of metastatic seeding in our models. For this, we injected 4T1-GFP cells i.v. and analyzed lungs at 12 and 48 h after injection (Figure S4A). We used confocal microscopy to quantify the numbers of GFP[+] colonies (defined as cell clusters of >100 μm) and individual cells per mm^2 of lung tissue (Figure S4B). We could not detect differences at 12 h after injection, indicating that the seeding might not be majorly affected by IL-22 (Figures S4C and S4D). However, at the 48-h time point, the numbers of GFP^{+} cells and colonies decreased in the lung of $Il22^{-/-}$ mice (Figures S4C and S4D). This suggested a role for IL-22 in driving early metastasis in the lungs.

To assess the rate of proliferation, we co-injected mice with 5-ethynyl-2′-deoxyuridine (EdU) 4 h before investigation at 12,

---

Figure 2. T cells are the primary source of IL-22 in the lung of tumor-bearing mice

(A) Intravenous model of E0771 lung metastasis in $Foxp3^{mRFP}Il17a^{GFP}Il22^{sgBFP}$ reporter mice.

(B) Gating strategy to identify CD4^{+}, CD8^{+}, and double-negative (DN) T cells, γδ T cells, CD3^{+}NK1.1^{+}, and CD3^{−}NK1.1^{+} cells in the lungs. Numbers represent the frequency of the parent gate.

(C) Breakdown of CD45^{+}IL-22^{+} cells by cell type as defined by the mean frequency of reported experiments.

(D) IL-17A and IL-22 production by CD4^{+} T cells (n = 5). Data are presented as mean ± SEM, and the representative experiment of two is shown. p values by Welch's t-test.

(E) Representative 3D render of the z stack confocal images of metastatic foci and normal tissue of precision-cut lung slices from $Foxp3^{mRFP}Il17a^{GFP}Il22^{sgBFP}$ mice injected with E0771 cells i.v. Fifteen fields of view of each type were acquired per mouse from 3 individual mice. The field of view is 160 × 160 μm; 20 slices with an interval of 1 μm were acquired; displayed grid step is 20 μm. $Il17a^{GFP}$ is depicted in green, $Il22^{sgBFP}$ in blue, CD4 PerCP-Cy5.5 staining in magenta, and TO-PRO-3 nuclear staining in red. Correlation between $Il17a^{GFP}$ and $Il22^{sgBFP}$ median fluorescence intensity (MFI) in the reporter cells in the metastatic foci. The number of reporter cells per field of view in the metastatic foci and normal tissue. Normalized CD4 PerCP-Cy5.5 MFI in $Il22^{sgBFP+}$ cells gated from the previous graph. Representative data are presented as means ± SEM of one animal of thee. p values <0.05 are considered significant as calculated by the unpaired t-test.

(F) Intravenous mouse model of E0771-GFP lung metastasis in $Il22^{flox}Cd4^{cre}$ mice. Representative dot plots, numbers of macroscopic metastases, and frequency of E0771-GFP cells in the lungs of WT and $Il22^{flox}Cd4^{cre}$ mice (n = 18). Data are presented as means ± SEM; three independent experiments were pooled. p values <0.05 are considered significant as calculated by the Mann-Whitney U test.

(G) Model of metastasis in $Rag1^{-/-}Il22^{-/-}$ that received WT or $Il22^{-/-}$ CD4^{+} T cells i.p. (2 × 10^6 per mouse) 28 days before i.v. tumor injection. Representative dot plots, numbers of macroscopic metastases, and frequency of E0771-GFP cells in the lungs (n = 5 and 4). Data are presented as means ± SEM of one experiment. p values <0.05 are considered significant as calculated by the Mann-Whitney U test. See also Figure S2.
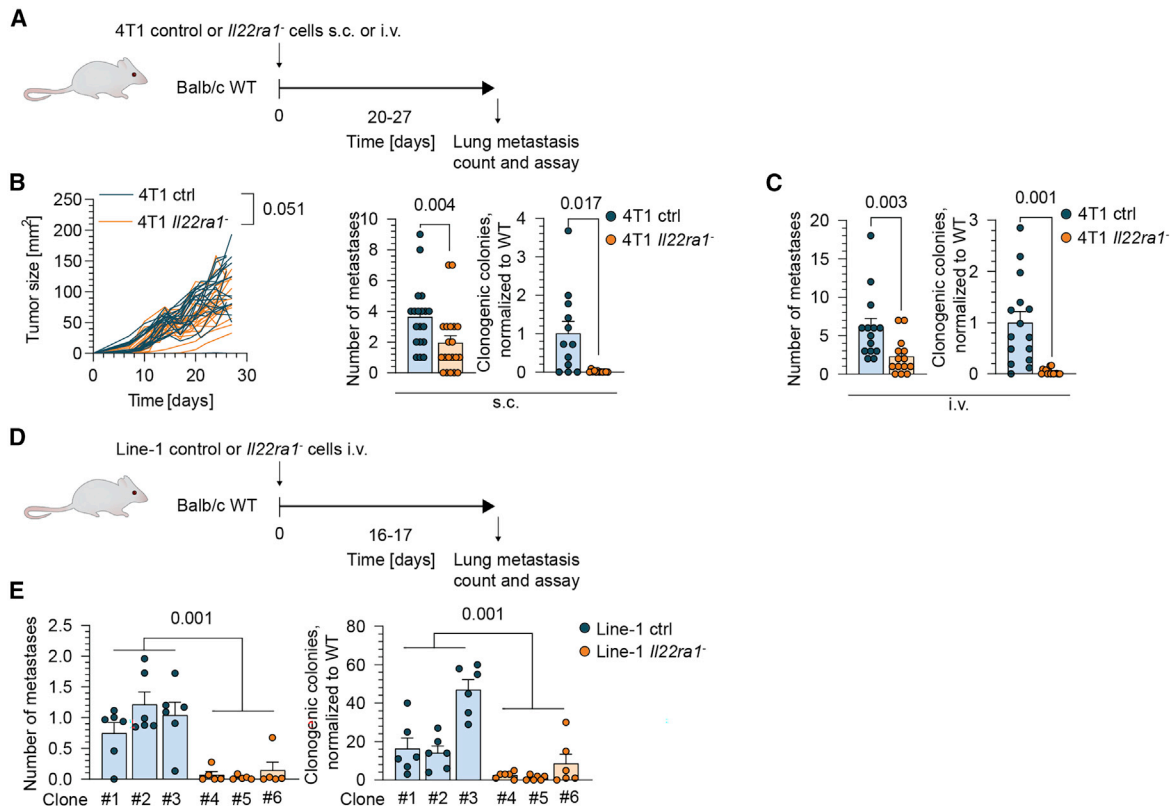
Figure 3. IL-22RA1 expression on tumor cells is indispensable for metastasis formation

(A) Subcutaneous and intravenous models of 4T1 *Il22ra1⁻* lung metastasis.

(B) Tumor size, number of metastases, and clonogenic colonies in s.c. model per animal (n = 20 and 21). Data from three independent experiments for tumor size and metastasis count and two for metastasis assay were pooled.

(C) Number of metastases and clonogenic colonies in i.v. model (n = 14). Data from three independent experiments were pooled.

(D) Intravenous model of Line-1 *Il22ra1⁻* lung metastasis.

(E) Number of metastases and colonies of the Line-1 control (#1, #2, #3) or *Il22ra1⁻* (#4, #5, #6) clones (n = 6 per clone). Data from two independent experiments were pooled and are presented as means ± SEM; p values <0.05 were considered significant by mixed-effect two-way analysis for tumor growth and by the Mann-Whitney U test for the number of metastases and colonies. See also Figures S3 and S4.

24, 48 h, and 7 days after tumor injection (Figure S4E). Similar to microscopic counting, we did not detect differences in the numbers of GFP⁺ cells earlier than 48 h after injection (Figures S4F–S4G). In contrast, we could detect differences in EdU incorporation, which indicates a higher fraction of dividing cells only by day 7 after injection (Figure S4G). Thus, we reason that differences in lung tumor burden affected by IL-22 observed as early as 48 h are mediated by a mechanism independent of proliferation.

IL-22 regulates the expression of CD155 on tumor cells and thereby promotes metastasis

Based on our findings that IL-22 acts on *IL-22ra1⁺* cancer cells to promote metastasis, we performed bulk RNA sequencing of 4T1 cells treated with IL-22 to further delineate the underlying mechanism (GEO: GSE202314) (Figure 4A). We discovered 147 genes that were differentially regulated. Of these, the expression of 133 genes was increased, and 14 decreased upon IL-22 treatment (Figures 4B and S5A). We validated *Pvr* (poliovirus receptor, Pvr) as one of the most significantly increased targets using qPCR (Figure S5B). This is notable

because CD155, the product of *Pvr*, is overexpressed in various cancers and possesses tumor-promoting properties, including metastasis.[54–56] To confirm our findings, we evaluated the expression of CD155 in IL-22-stimulated 4T1, Line-1, and E0771 cells by flow cytometry (Figure 4C). We detected an increase in the expression of CD155 in all cell lines over 72 h (Figures 4D and 4E), but this effect was absent in cells lacking IL-22RA1 (Figure S5C). Next, we evaluated the impact of IL-22 on CD155 expression in E0771-GFP cells from the lungs of tumor-bearing mice (Figure 4F). Here, we could confirm that cells implanted into *Il22⁻/⁻* mice had a lower expression of CD155, which correlated with a smaller fraction of E0771-GFP cells detected by flow cytometry (Figures 4G and 4H).

To verify the role of CD155 in metastasis, we established *Pvr⁻* Line-1 and 4T1 cell lines (Figures 4I, S5D, and S5G). While this had little effect on their capacity to grow subcutaneously (Figures S5E and S5F), it abolished the ability to form metastases in the lung (Figures 4J and S5H). We could reverse this process by constitutive CD155 expression in *Pvr⁻* cells independently of IL-22-induced regulation (*Pvr⁺*).
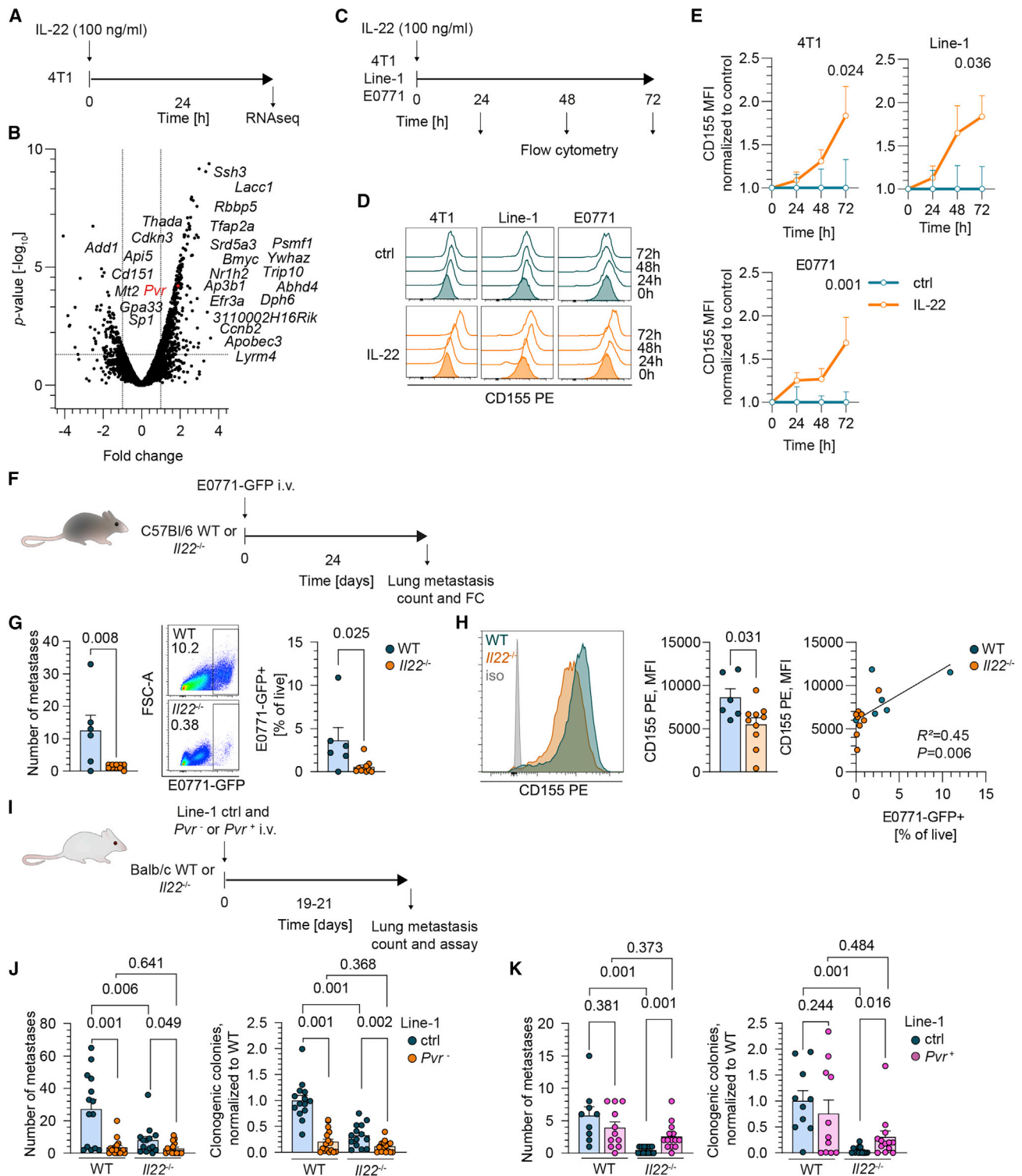
Figure 4. IL-22 signaling increases the expression of CD155 on the surface of tumor cells and confers resistance to metastasis control

(A) 4T1 cells were stimulated with IL-22 (100 ng/mL) for 24 h *in vitro* before bulk mRNA sequencing.

(B) The volcano plot depicts the fold change and adjusted p values of differentially regulated genes. One hundred forty-seven genes were discovered as defined by an adjusted p value threshold of 0.05 and Log_2 fold change of ±1.

(C) CD155 expression in 4T1, Line-1, and E0771 cells after stimulation with rmIL-22 (100 ng/mL) for 72 h *in vitro*.

(D) Representative histograms of CD155 expression at 24, 48, and 72 h.

(legend continued on next page)

In this setting, we could induce metastases in the lungs of $Il22^{-/-}$ mice, highlighting the link between these two molecules and their role as mediators of the metastatic process (Figures 4K and S5I).

CD155 on tumor cells is associated with decreased expression of CD226 on NK cells and reduced IFNγ production

CD155 plays an intrinsic role in proliferation and adhesion in cancer cells,[54–57] among others. We did not detect deficiencies in the proliferation of Line-1 Pvr^- cells in vitro (data not shown). Importantly, CD155 has a cell-extrinsic pro-metastatic role by binding to the immunomodulatory receptors CD96, CD226, or TIGIT on the surface of NK and T cells.[54–56,58,59] To pinpoint the binding partners of CD155, we analyzed anti-tumor responses in the lungs of mice containing 4T1-luciferase$^+$ cells (4T1-Luc) (Figure 5A). We confirmed using an in vivo imaging system (IVIS) that wild-type and $Il22^{-/-}$ mice had similar seeding of tumor cells by day 5 after injection, and the differences in tumor burden increased over the course of two weeks (Figures 5B and 5C). Indeed, the defect of IFNγ production by NK cells, but not other cell types, showcased the loss of humoral effector mechanisms (Figures 5D, 5E, and S6A) and correlated with higher tumor burden (Figure S6B). This effect was consistently found in the Line-1 s.c. model (Figures S6C–S6E). Scrutinized by chip cytometry,[60] samples from 4T1-lung metastasis-bearing mice demonstrated increased expression of CD155 in the metastatic foci in WT but not in $Il22^{-/-}$ animals (Figures 5F and S6F). We found higher infiltration of NK cells into the metastatic foci of $Il22^{-/-}$ but not WT animals, suggesting higher activation and confirming the dependency on NK cells as anti-tumor effector cells (Figure 5F).

CD226, but not TIGIT or CD96, was differentially expressed by NK cells and, to a lesser extent, by CD8$^+$ T cells in the lungs of wild-type and $Il22^{-/-}$ animals (Figures 5G and S6G–S6H). CD226 is a co-receptor essential for the activation of effector functions of NK and CD8 T cells. Therefore, we set out to explore its pathophysiological relevance in our model.[61–64]

Blockade of CD226 abrogates the anti-metastatic phenotype of IL-22-deficient animals

Excessive CD155-mediated signaling present in the tumor microenvironment can induce internalization and degradation of CD226 in effector cells.[61,63] To delineate the role of excessive CD155 expression on CD226 and subsequent anti-tumor response, we injected 4T1 control and Pvr^+ cells i.v. in $Il22^{-/-}$ mice, and two groups also received anti-CD226 blocking antibody (480.1) (Figure 6A). Both Pvr^+ cells and CD226 blockade could similarly promote lung metastasis in $Il22^{-/-}$ mice, and

these effects did not synergize (Figure 6B). Similar to our previous observations in wild-type animals, this was sufficient to inhibit IFNγ production by NK cells (Figure 6C). Finally, we detected a decrease in CD226 expression on NK cells in Pvr^+-injected mice compared with control cells. This correlated with decreased capacity of these NK cells to produce IFNγ (Figure 6D). Furthermore, we interrogated the potential of agonistic TIGIT antibody (IG9) to inhibit NK cell activation in $Il22^{-/-}$ animals and of CD96 blockade (3.3) to prevent the inhibition of NK cell function (Figure 6E). Neither TIGIT agonist nor CD96 antagonist altered the number of metastases when compared with $Il22^{-/-}$ animals that received control or Pvr^+ 4T1 cells, respectively (Figure 6F). When activated, TIGIT could inhibit IFNγ production from CD8$^+$ T but not NK cells (Figure 6G). Thus, an IL-22-CD155 axis triggers decreased expression of CD226 in NK cells and renders them inert in the tumor microenvironment.

CD155 expression complements the IL-22 gene signature in breast and lung cancer patients

Finally, we assessed the clinical relevance of CD155 in the context of the IL-22-IL-22RA1 axis. CD155 expression alone is associated with unfavorable prognosis in a variety of cancer entities.[54] We analyzed RNA sequencing data from the cancer genome atlas (TCGA) lung adenocarcinoma (TCGA: LUAD, n = 504) and HER2-positive patient samples from the invasive breast carcinoma (TCGA: BRCA, n = 110) datasets. We focused on key IL-22-related genes: $IL22RA1$, $IL22RA2$, $IL10RB$, and PVR. To stratify patient cohorts, we utilized agglomerative clustering, an unsupervised clustering method, resulting in three major clusters (Figures 7A and 7B). This revealed distinctive gene expression patterns: cluster 0 ($IL22RA1^{hi}$, $IL22RA2^{lo}$, $IL10RB^{med}$, PVR^{hi}), cluster 1 ($IL22RA1^{lo}$, $IL22RA2^{hi}$, $IL10RB^{hi}$, PVR^{lo}), and cluster 2 ($IL22RA1^{lo}$, $IL22RA2^{lo}$, $IL10RB^{lo}$, PVR^{med}) (Figure 7C). These clusters were evenly distributed in these two cohorts (Figure 7D). Patients in cluster 0 and LUAD dataset cluster 2 had worse survival than patients in cluster 1 (Figure 7E). Survival of clusters 1 and 2 did not differ in both cohorts (Figure 7E). Further, we calculated restricted mean survival times (RMST) for clusters 0 and 1 to quantify the difference in expected survival time until five years of follow-up, resulting in −361.18 days for LUAD and −93.23 days for BRCA (Figure 7F). Clusters 0 and 1 had differences in the frequency of pathologic disease stages within them in the LUAD but not in the BRCA cohort (Figure 7G). Importantly, such survival differences between clusters ($IL22RA1^{hi}PVR^{hi}$) and 1 ($IL22RA1^{lo}PVR^{lo}$) mainly stem from patients diagnosed at the early (I and II), but not at advanced, stages of the disease (III and IV) (Figure S7A). To assess the impact of each gene on survival, we utilized Cox's proportional hazards model. Both $IL22RA1$ (hazard ratio [HR] = 1.23) and

(E) MFI of CD155-PE signal normalized to control (n = 3). Data are presented as means ± SEM, and p values <0.05 are considered significant as calculated by the mixed model two-way analysis.

(F) Intravenous model of E0771-GFP lung metastases in WT and $Il22^{-/-}$ mice.

(G) Numbers of metastases in the lungs, representative plots, and frequency of E0771-GFP$^+$ cells (n = 6 and 10). The numbers are the frequency of the parent gate.

(H) Representative histogram and MFI of CD155 staining of GFP + tumor cells. Linear regression analysis of CD155 MFI and frequency of E0771-GFP + tumor cells. Data from one experiment. p values are calculated by the Mann-Whitney U test.

(I) Intravenous models of Line-1 Pvr^- and Pvr^+ metastasis in WT and $Il22^{-/-}$ mice.

(J and K) Numbers of metastases and colonies in metastasis assay of (J) Line-1 Pvr^- and (K) Pvr^+ cells. Data from three independent experiments for Pvr^- and two experiments for Pvr^+ were pooled and are presented as means ± SEM; p values <0.05 were considered significant by the Mann-Whitney U test. See also Figure S5.
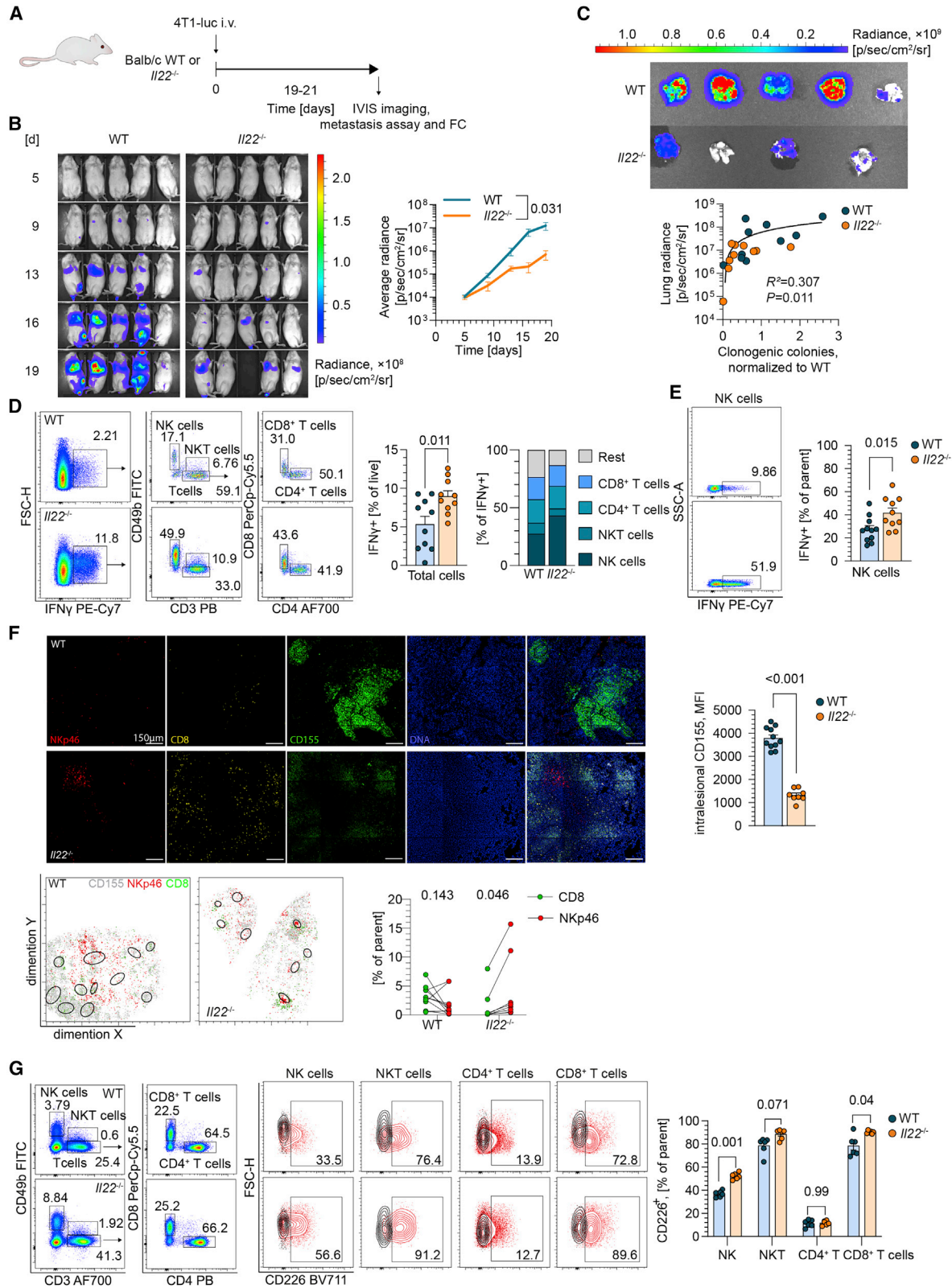
Figure 5. CD226 expression is higher on NK cells in *Il22*⁻/⁻ mice

(A) Intravenous model of 4T1-luciferase⁺ (4T1-Luc) metastasis.

(B) Representative IVIS images and average radiance from one experiment of two (n = 5).

PVR (HR = 1.28) impact survival, whereas *IL22RA2* and *IL10RB* did not change the hazard in the LUAD cohort (Figure S7B). Moreover, only *CD226* (p = 0.06), but not *TIGIT* or *CD96*, trended to influence the survival, in line with our findings in preclinical models (Figure S7B).

We used the CIBERSORTx deconvolution algorithm on the LUAD cohort to assess whether gene expression patterns of our clusters have an impact on immune cell infiltration in patients.[65] Interestingly, there is an increase in CIBERSORTx units for activated NK cells in cluster 1 when compared with clusters 0 and 2 in LUAD patients, whereas there were no differences in resting NK cells or activated CD4^{+} memory T cells (Figure S7C) with a similar trend in the BRCA cohort (Figure S7D).

Together, these results from clinical cohorts demonstrate the relevance of a regulatory link between T cell-derived IL-22 and CD155.

DISCUSSION

In this study, we discovered a mechanism by which T cells produce IL-22 to promote lung metastasis in mouse models of lung and breast cancer. Mechanistically, T cells at the metastatic foci in the lung, predominantly CD4^{+}, produce IL-22 that signals directly through its receptor expressed in cancer cells, promoting expression of the pro-metastatic molecule CD155.[54-56,58,59] Despite the well-studied pan-cancer expression of CD155 and its intrinsic and extrinsic roles in cancer progression,[54] the pathway responsible for CD155 regulation in malignant cells remains elusive.[66–68] We demonstrated that IL-22 increased CD155 expression in lung and breast cancer cell lines *in vitro* and *in vivo*, whereas its constitutive expression enabled metastases in *Il22*^{−/−} mice, compared with control and deficient cells. Increased expression of CD155 in the tumor lung microenvironment led to a reduction of co-stimulatory molecule CD226 on NK cells, diminishing their localization to metastases and IFNγ production, which correlated with higher tumor burden.

In our previous studies, we detected an accumulation of IL-22-producing T cells in non-small-cell lung carcinoma (NSCLC) patient tumor samples.[12,48] We have demonstrated that cancer cells trigger NLRP3-dependent secretion of IL-1β that induces such IL-22 production mainly from Th cells.[18] Worth noting is that, in humans, due to the differences in the Th cell cytokine profiles, IL-22 is also induced in Th1 cells. It is conceivable that this might impair the anti-tumor immune response. Importantly, such Th1 variants might partially explain cancer hyperprogression upon T cell activation following checkpoint blockade.[69]

In line with our previous observations, we confirmed the accumulation of IL-22-producing CD4^{+} and CD8^{+} T cells, but also NK1.1^{+} cells, in the metastatic niche in the lung of tumor-injected animals. It is important to note that we observed strain-specific differences in the accumulation of such IL-22-producing CD8^{+} T cells across our models. However, abolishing the IL-22 production in total mature T cells was sufficient to recapitulate the effect we observed in IL-22-deficient animals.[70] Also, the adoptive transfer of CD4^{+} T cells into *Rag*^{−/−}*Il22*^{−/−} mice was sufficient to induce lung metastases, pinpointing the paramount role of Th cells as a source of IL-22. Conversely, our previous findings suggest that despite an accumulation of CD8^{+} T cells in tumor samples, their contribution to the IL-22 pool is minor.[48] In any case, the characterization of such CD8^{+} IL-22-producing T cells is essential to carefully evaluate their pro- or anti-tumor properties as new data on this subpopulation emerges.[71,72] Also, the primary role of NK and NKT cells in tumor control outweighs their potential contribution to metastasis formation through IL-22, which is discerned in a *Rag*^{−/−}*Il22*^{−/−} adoptive transfer experiment using animals devoid of mature T cells but having functional NK cells.[37] This hypothesis is further supported by our findings in the metastatic foci where NK cells were found more abundantly than cytotoxic T cells, highlighting NK cells as essential players in tumor control in the absence of IL-22.

It is important to note that we focused on IL-22 producers at metastatic foci in the lung but do not consider their origin, clonality, or their distribution in blood or lymphoid organs. Moreover, various sources of IL-22 promote tumor progression in a context-dependent manner mediated by the pleiotropic action of this cytokine. Along these lines, similar IL-22-producing cells in various compartments (lung vs. spleen vs. lymph node) could differentially affect pro-tumoral phenotypes or have no function depending on the context, which will need to be investigated further.

Cancer studies repeatedly report that IL-22 affects the development and growth of primary tumors and, eventually, neoplastic progression.[26,73–76] This notion is mainly justified by the ability to promote migration, invasion, and stemness of cancer cells *in vitro* and thus promote metastasis formation.[76,77] Importantly, ablation of IL-22 can alleviate the immunosuppressive microenvironment in a *Kras*-mutant model of lung carcinoma.[14] In the current study, we demonstrated that the increased metastatic burden was a direct effect of IL-22 on disseminated IL-22RA1^{+} tumor cells, which resulted in increased colony outgrowth. Importantly, our data do not formally rule out an impact on non-tumor cells. As such, the influence of IL-22 on tumor cell dissemination through the intrinsic action of endogenously expressed IL-22R is extensively highlighted by Giannou et al.[78]

(C) *Ex vivo* imaging of the lung by IVIS. Linear regression analysis of clonogenic colonies vs. average radiance.

(D) Representative dot plots and gating strategy of IFNγ-producing cells in the lungs. Numbers represent the frequency of the parent gate. Frequency of IFNγ^{+} cells in the lung and composition by cell type including CD8^{+} and CD4^{+} T cells, NKT cells, and NK cells.

(E) Representative dot plots and frequency of IFNγ^{+} NK cells (n = 9 and 10). Data from two independent experiments were pooled.

(F) Representative fluorescent microscopy images of lungs from 4T1-injected mice. NKp46 FITC signal is depicted in red, CD8 AF555 in yellow, CD155 PE in green, and Hoechst DNA staining in blue. Intralesional CD155 PE MFI per lesion in WT and *Il22*^{−/−} mice. Chip cytometry spatial distribution of NKp46^{+} (red), CD8^{+} (green), and CD155^{+} (gray) cells in the microscopy samples. Frequency of CD8 and NKp46 cells per lesion from the previous graph. Data presented as means ± SEM; p values <0.05 were considered significant by paired t test of one chip of 2 for each condition (n = 3 and 4).

(G) Gating strategy and representative plots of CD226 staining on CD8^{+} T, CD4^{+} T, NKT, and NK cells. Isotype control is in black. Frequency of CD226^{+} cells in the lungs (n = 6). Data of one experiment of two. Data presented as means ± SEM; p values <0.05 were considered significant by the Mann-Whitney U test or multiple unpaired t tests with Holm-Sidak correction. See also Figure S6.
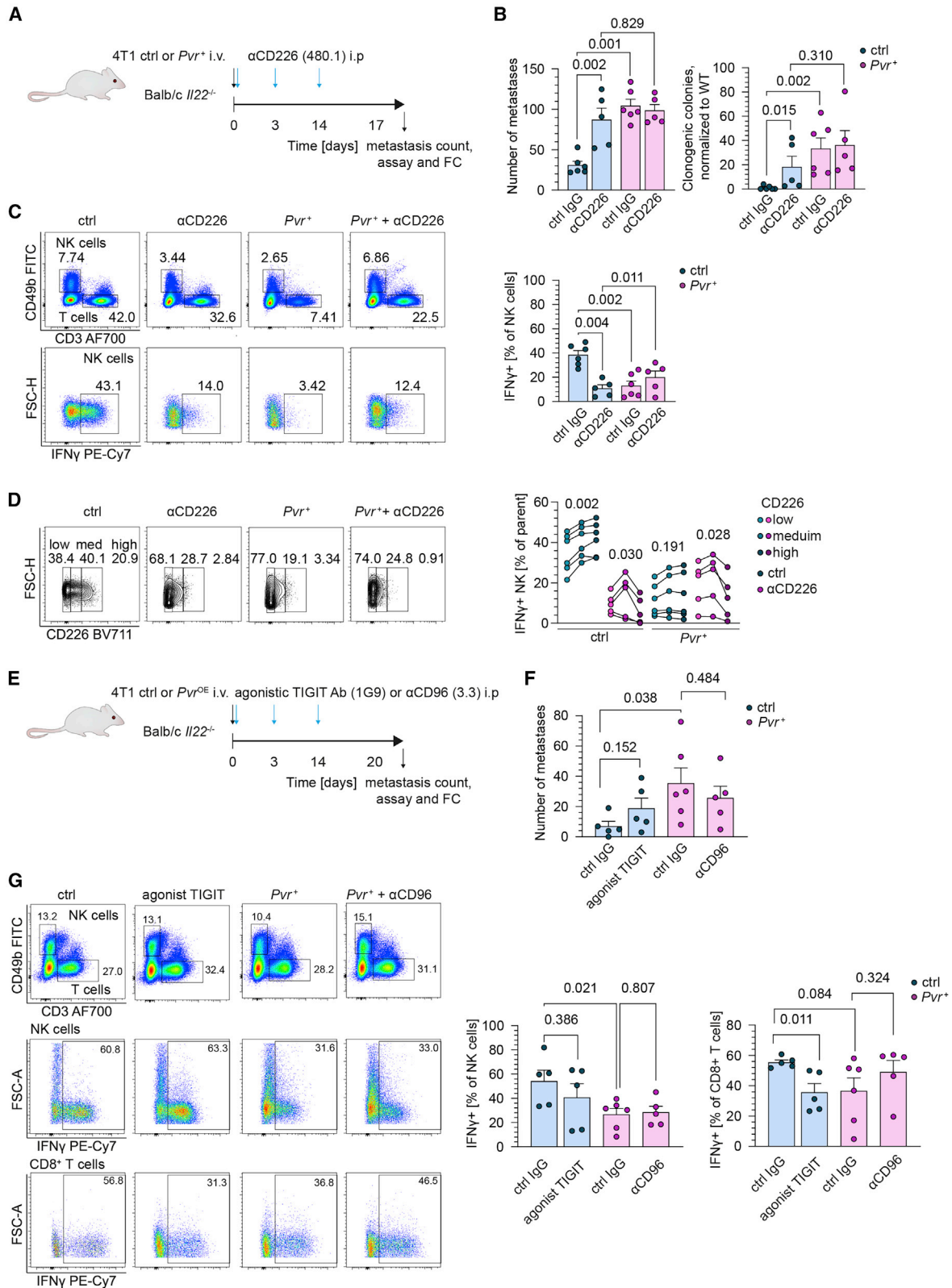
Figure 6. CD226 signaling is indispensable for IFNγ production from NK cells

(A) Intravenous mouse model of 4T1 control or *Pvr*+ metastasis in *Il22*−/− mice. Animals received injections of anti-CD226 blocking antibody (420.1, 200 μg per mouse) or control i.p. on days 0, 3, and 14.

(legend continued on next page)

We demonstrated that *Pvr* is one of the genes with increased expression on cancer cells upon IL-22 treatment. In this context, CD155-deficient cells formed few metastases, both in wild-type and *Il22*−/− mice, and, importantly, the reintroduction of CD155 allowed us to reconstitute the metastatic phenotype. The intrinsic role of CD155 in cancer cells has been well studied and is known to affect seeding, tumor cell proliferation, and migration.[56,57] However, *Pvr*− cells did not display inhibited proliferation or migration in our hands, and the seeding of tumor cells was unaffected in *Il22*−/− mice. Initially identified on antigen-presenting cells, CD155 serves as an extrinsic promotor of tumor progression that suppresses NK and T cell function by binding to CD96 and TIGIT on their surface and induces internalization and downregulation of CD226.[56,61–64,79–85] Due to its immunosuppressive function, CD155 in cancer and host cells exerts pro-metastatic properties and is proposed as a target for checkpoint inhibition blockade.[61,86] NK cells receive a co-stimulatory signal from antigen-presenting cells via CD226.[87] However, excessive stimulation of CD226 in the tumor microenvironment leads to internalization and degradation.[63] This is typically counteracted by CD96 and TIGIT, which bind CD155 with a higher affinity.[58] Interestingly, 4T1 cells are known to induce CD226 downregulation in tumor-infiltrating lymphocytes and suppress IFNγ production.[88] Here, we demonstrated that IL-22 deficiency preserved CD226 expression on NK and CD8+ T cells. However, only NK cells had dramatically higher IFNγ production capabilities and inversely correlated with metastatic burden. Interestingly, activation of TIGIT signaling in our study inhibited IFNγ production from CD8+ T, but not NK, cells and was not sufficient to increase the metastatic burden. Similarly, another receptor for CD155, CD96, was neither differentially regulated in *Il22*−/− mice nor did inhibition thereof prevent metastasis, indicating that CD155 does not suppress NK cells via CD96 in our model. This highlights cell type-specific regulation of anti-tumor responses by CD155 and its various binding partners.

The impact of CD155 on the prognosis and its role in the pathogenesis of lung, breast, colon, and other types of cancer is established.[79–85] There is vast evidence on the prognostic relevance of IL-22 and its related genes in various cancer entities.[10,21,27,75,89–91] However, some studies report no influence of IL-22 expression on survival.[12] While these discrepancies might be due to the heterogeneity in patient populations, sampling, and reporting issues, many of these studies focus on a single gene related to IL-22 signaling. Here, we utilized agglomerative clustering to discern expression patterns of *IL22RA1*, *IL22RA2*, *IL10RB*, and *PVR* in LUAD and BRCA cohorts in TCGA and affiliate them with the clinical data. Here, we identified three patterns of expression of these genes: pattern 0 (*IL22RA1*hi, *IL22RA2*lo, *PVR*hi), pattern 1 (*IL22RA1*lo, *IL22RA2*hi, *PVR*lo), and pattern 2 (*IL22RA1*lo, *IL22RA2*lo, *PVR*med). We identified that

high expression of the *IL22RA1* coincided with a high expression of *PVR*, which also translated into poor overall survival outcomes, particularly in patients diagnosed with early (I and II), but not advanced (III and IV), pathological stages, highlighting the stage-specific role of this mechanism. Conversely, high expression of *IL22RA2*, also known as IL-22BP, was correlated with lower *PVR* expression and better survival.[18,34] The third pattern corresponded to all-low expression and represented immunologically cold tumors.[92] Along these lines, CIBERSORTx deconvolution indicated that cluster 1 characterized by high *IL22RA2* expression features a gene signature for activated, but not resting, NK cells compared with other clusters.

CD226 expression is demonstrated to stratify patients for outcome in several NSCLC clinical trials.[93] However, due to the dual way of pre- and post-translational regulation of CD226, expression is not always reflected in mRNA sequencing data.[94] Hence, studies that focus on the post-translational regulation of CD226 evaluate its expression in clinical samples using antibody staining.[63] Nevertheless, when interrogating the TCGA dataset concerning the relationship of CD155 binding partners to survival, only *CD226* trended toward bettering prognosis (log (HR) = −0.24, p = 0.06), whereas *TIGIT* and *CD96* demonstrated no correlation with survival.

Importantly, tumor cells engineered to secrete IL-22BP formed fewer metastases, highlighting the potential of the IL-22 pathway for targeted therapeutic intervention. This could counteract tumor CD155 overexpression, as direct targeting of which remains challenging due to a complex network of co-receptors. Of further note, the long-term effects of IL-22 neutralization on metastasis are unknown but could have a direct impact on the therapeutic consideration of T cells or provide the rationale for IL-22 neutralization using antibodies with a beneficial safety profile, such as Fezakinumab (trial NCT01941537) or engineered IL-22 with structure-based design.[39,95]

In summary, we identified IL-22-induced CD155 overexpression on the tumor cells as a mechanism that benefits metastatic outgrowth. This essential role in prognosis stressed the potential of IL-22 as a therapeutic target in cancer. So far, the neutralization of IL-22 is proposed mainly as a strategy to treat autoimmune diseases.[31,49] Our data on IL-22BP as a neutralizer of IL-22, which phenocopied the global IL-22 deficiency, underpinned the therapeutic potential for targeting the IL-22-IL-22R1 axis and should be further explored in preclinical and clinical studies.

LIMITATIONS OF THE STUDY

Despite the potential relevance of the IL-22 pathway for patients' outcomes, the analysis is based on primary tumor data and thus might miss divergent impacts at later stages. Along these

(B) Numbers of macroscopic lung metastases and colonies in metastasis assay.

(C) IFNγ-producing NK cells in the lungs evaluated by flow cytometry. Data presented as means ± SEM; p values <0.05 were considered significant by the Mann-Whitney U test.

(D) Representative dot plots depict CD226 low, medium, and high NK cells. Frequency of IFNγ+ cells among NK cell populations (n = 5–6). Numbers represent the frequency of the parent gate. Data presented as means ± SEM; p values <0.05 were considered significant by the two-way ANOVA.

(E) Intravenous mouse model of 4T1 control or *Pvr*+ lung metastasis in *Il22*−/− mice. Animals received injections of anti-TIGIT agonist antibody (1G9, 250 μg per mouse), anti-CD96 blocking antibody (3.3, 250 μg per mouse), or control i.p. on days 0, 3, and 14.

(F) Numbers of macroscopic lung metastases.

(G) IFNγ-producing NK and CD8+ T cells in the lungs were evaluated by flow cytometry. Numbers represent the frequency of the parent gate. Data presented as means ± SEM; p values <0.05 were considered significant by unpaired t-test (n = 5–6).
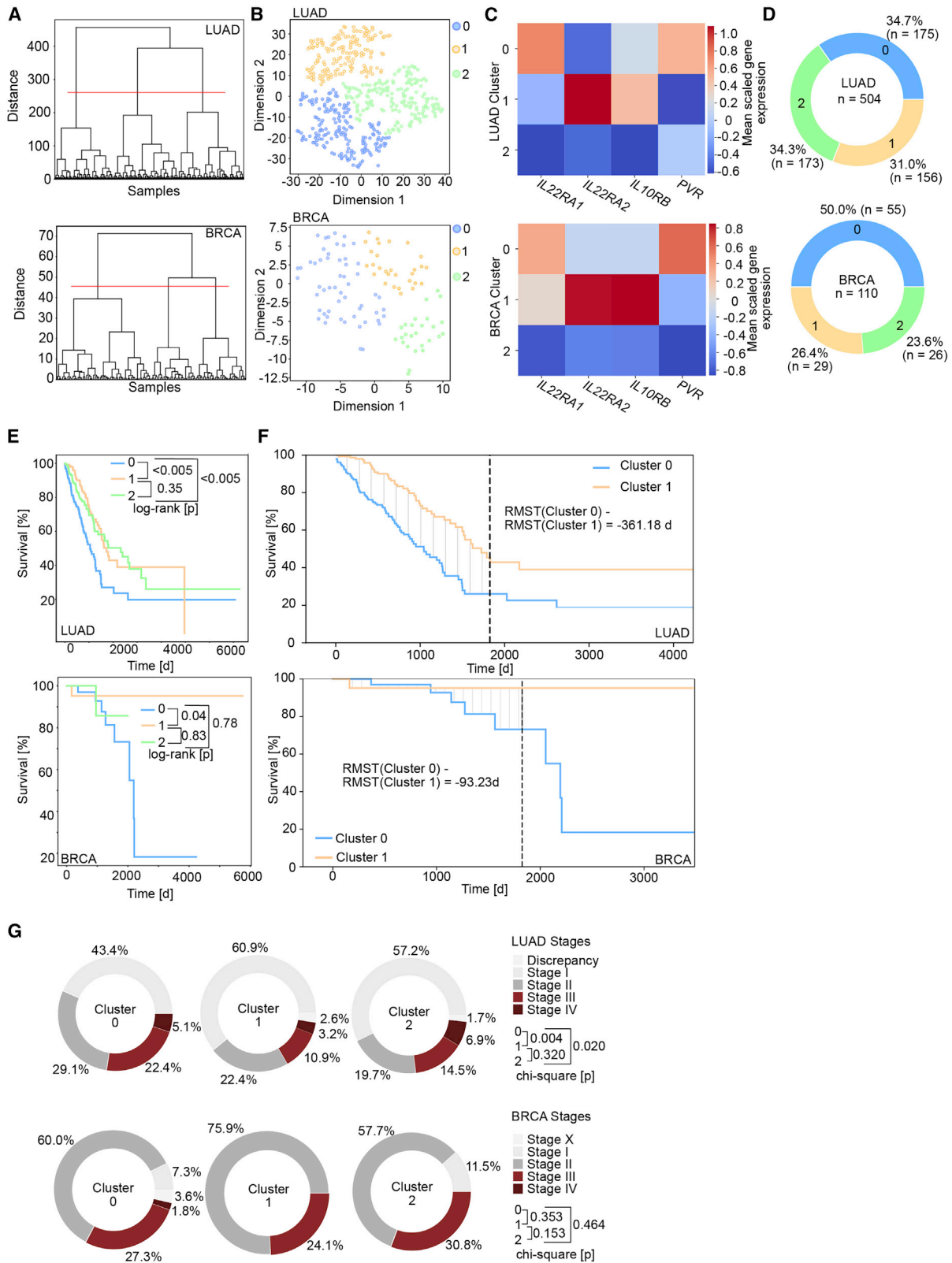
(legend on next page)

lines, findings will need to be evaluated additionally in human metastasis. Also, we present a study on IL-22-mediated immunosuppression in the lung but could also demonstrate a similar effect in a forced model of liver metastasis. In contrast, as suggested by Giannou et al.,[78] there are organ-specific variations in the source and dominant mechanism of IL-22-induced metastasis, which must be considered. Lastly, we could detect strain-specific differences in IL-22 production from CD8^{+} T cells in our models. This, and the ability of Th1 cells to serve as the source of IL-22 in human, may suggest varying outcomes and must be considered when translating these findings to patients.

STAR★METHODS

Detailed methods are provided in the online version of this paper and include the following:

- KEY RESOURCES TABLE
- RESOURCE AVAILABILITY
  - Lead contact
  - Materials availability
  - Data and code availability
- EXPERIMENTAL MODEL AND SUBJECT DETAILS
  - Mice
  - Cell lines
  - Mouse tumor models
  - Intrasplenic (i.s.) tumor cell injection
  - Adoptive T cell transfer
  - Quantification of macrometastasis and single-cell isolation from the lung
  - Clonogenic metastasis assay
  - *In vivo* imaging
- METHOD DETAILS
  - Generation of 4T1-GFP and E0771-GFP cell lines
  - Generation of IL-22BP-producing (*Il22ra2*^{+}) cells
  - Generation of *Il22ra1*[-] and *Pvr*[-] cell lines using CRISPR/Cas9 system
  - Next-generation sequencing
  - Short read mapping
  - Differential expression analysis
  - RNA isolation and RT-qPCR
  - Flow cytometry
  - Generation of Th17 cells from mouse splenocytes
  - Proliferation assessment using EdU
  - Confocal microscopy
  - iDISCO tissue clearing and light-sheet microscopy
  - Precision-cut lung slices (PCLS) and confocal microscopy
  - H&E staining

- Chip cytometry
- Chip cytometry image processing and segmentation
- TCGA data analysis
- Deconvolution analysis
- QUANTIFICATION AND STATISTICAL ANALYSIS

SUPPLEMENTAL INFORMATION

Supplemental information can be found online at https://doi.org/10.1016/j.immuni.2022.12.010.

Figure 7. Cluster stratification and clinical outcome of LUAD and BRCA patient samples based on IL-22-CD155 signature genes

(A) Dendrogram of agglomerative clustering of TCGA LUAD and BRCA HER2+ datasets based on *IL22RA1*, *IL22RA2*, *IL10RB*, and *PVR* expression.

(B) t-distributed Stochastic Neighbor embedding (t-SNE) dimensionally reduced scaled gene expression values. Each dot represents one patient sample, and colors indicate cluster affiliation.

(C) Heatmap of the mean scaled expression of *IL22RA1*, *IL22RA2*, *IL10RB*, and *PVR* per cluster.

(D) Relative proportions of the clusters.

(E) Kaplan-Meier survival plots of all clusters for each dataset respectively. Log rank (Mantel-Cox) test was used to compare curves.

(F) Restricted mean survival time difference (δRMST) of clusters 0 and 1. Line indicates a cutoff of 1,825 days.

(G) Frequency of summarized pathologic stages per cluster. A chi-squared test was used to compare groups; p values <0.05 are considered significant. All shown results were generated in one representative run of the analysis script.

AUTHOR CONTRIBUTIONS

Conceptualization, D.B., J.S.-G., C.V., A.M., J.J., M. Schübel, J.D., F.M., P.M., A.G., N.T., A.D.G., T.B., J.L., L.M.K., B.L.C., H.-J.A., S.R., D.C.-W., C.T., M.S.S., R.A.F., S.E., S.K.; methodology, N.T., L.M.K., S.R., D.C.-W., C.T., M.S.S., B.L.C., O.M., M.H.; investigation, D.B., J.S.-G., C.V., A.M., J.J., M. Schübel, J.D., F.M., P.M., A.G., N.T., A.D.G., J.L., T.Z., A.O., M. Schwerdt-feger, P.J.M., R.G., M. Seifert, M.H., O.M., B.L.C., L.M.K., D.A.-S., and S.M.; writing and visualization, D.B., J.J., J.S.-G., M. Schwerdtfeger, N.T., J.L., L.M.K., D.A.-S., B.L.C., H.-J.A., S.R., and S.K.; funding acquisition, L.M.K., S.R., S.H., S.K., and S.E.; resources, L.M.K., S.R., S.H., R.A.F., S.E., and S.K.; supervision, S.E. and S.K.

DECLARATION OF INTERESTS

REFERENCES

1. Hanahan, D., and Weinberg, R.A. (2011). Hallmarks of cancer: the next generation. Cell 144, 646–674. https://doi.org/10.1016/j.cell.2011.02.013.

2. Massagué, J., and Obenauf, A.C. (2016). Metastatic colonization by circulating tumour cells. Nature 529, 298–306. https://doi.org/10.1038/nature17038.

3. Renner, P., Rovira, J., Klein, C., Schlitt, H.J., Geissler, E.K., and Kroemer, A. (2014). KLRG1(+) natural killer cells protect against pulmonary metastatic disease by immunosurveillance. OncoImmunology 3, e28328. https://doi.org/10.4161/onci.28328.

4. Mohme, M., Riethdorf, S., and Pantel, K. (2017). Circulating and disseminated tumour cells - mechanisms of immune surveillance and escape. Nat. Rev. Clin. Oncol. 14, 155–167. https://doi.org/10.1038/nrclinonc.2016.144.

5. Briukhovetska, D., Dörr, J., Endres, S., Libby, P., Dinarello, C.A., and Kobold, S. (2021). Interleukins in cancer: from biology to therapy. Nat. Rev. Cancer 21, 481–499. https://doi.org/10.1038/s41568-021-00363-z.

6. Kitamura, T., Qian, B.Z., and Pollard, J.W. (2015). Immune cell promotion of metastasis. Nat. Rev. Immunol. 15, 73–86. https://doi.org/10.1038/nri3789.

7. Galon, J., and Bruni, D. (2020). Tumor immunology and tumor evolution: intertwined histories. Immunity 52, 55–81. https://doi.org/10.1016/j.immuni.2019.12.018.

8. Pagès, F., Mlecnik, B., Marliot, F., Bindea, G., Ou, F.S., Bifulco, C., Lugli, A., Zlobec, I., Rau, T.T., Berger, M.D., et al. (2018). International validation of the consensus Immunoscore for the classification of colon cancer: a prognostic and accuracy study. Lancet 391, 2128–2139. https://doi.org/10.1016/S0140-6736(18)30789-X.

9. Rui, J., Chunming, Z., Binbin, G., Na, S., Shengxi, W., and Wei, S. (2017). IL-22 promotes the progression of breast cancer through regulating HOXB-AS5. Oncotarget 8, 103601–103612. https://doi.org/10.18632/oncotarget.22063.

10. Kryczek, I., Lin, Y., Nagarsheth, N., Peng, D., Zhao, L., Zhao, E., Vatan, L., Szeliga, W., Dou, Y., Owens, S., et al. (2014). IL-22(+)CD4(+) T cells promote colorectal cancer stemness via STAT3 transcription factor activation and induction of the methyltransferase DOT1L. Immunity 40, 772–784. https://doi.org/10.1016/j.immuni.2014.03.010.

11. Jiang, R., Tan, Z., Deng, L., Chen, Y., Xia, Y., Gao, Y., Wang, X., and Sun, B. (2011). Interleukin-22 promotes human hepatocellular carcinoma by activation of STAT3. Hepatology 54, 900–909. https://doi.org/10.1002/hep.24486.

12. Kobold, S., Völk, S., Clauditz, T., Küpper, N.J., Minner, S., Tufman, A., Düwell, P., Lindner, M., Koch, I., Heidegger, S., et al. (2013). Interleukin-22 is frequently expressed in small- and large-cell lung cancer and promotes growth in chemotherapy-resistant cancer cells. J. Thorac. Oncol. 8, 1032–1042. https://doi.org/10.1097/JTO.0b013e31829923c8.

13. Hernandez, P., Gronke, K., and Diefenbach, A. (2018). A catch-22: interleukin-22 and cancer. Eur. J. Immunol. 48, 15–31. https://doi.org/10.1002/eji.201747183.

14. Khosravi, N., Caetano, M.S., Cumpian, A.M., Unver, N., De la Garza Ramos, C., Noble, O., Daliri, S., Hernandez, B.J., Gutierrez, B.A., Evans, S.E., et al. (2018). IL22 promotes Kras-mutant lung cancer by induction of a protumor immune response and protection of stemness properties. Cancer Immunol. Res. 6, 788–797. https://doi.org/10.1158/2326-6066.CIR-17-0655.

15. Li, H., Mou, Q., Li, P., Yang, Z., Wang, Z., Niu, J., Liu, Y., Sun, Z., Lv, S., Zhang, B., and Yin, C. (2019). MiR-486-5p inhibits IL-22-induced epithelial-mesenchymal transition of breast cancer cell by repressing Dock1. J. Cancer 10, 4695–4706. https://doi.org/10.7150/jca.30596.

16. Kim, K., Kim, G., Kim, J.Y., Yun, H.J., Lim, S.C., and Choi, H.S. (2014). Interleukin-22 promotes epithelial cell transformation and breast tumorigenesis via MAP3K8 activation. Carcinogenesis 35, 1352–1361. https://doi.org/10.1093/carcin/bgu044.

17. Katara, G.K., Kulshrestha, A., Schneiderman, S., Riehl, V., Ibrahim, S., and Beaman, K.D. (2020). Interleukin-22 promotes development of malignant lesions in a mouse model of spontaneous breast cancer. Mol. Oncol. 14, 211–224. https://doi.org/10.1002/1878-0261.12598.

18. Huber, S., Gagliani, N., Zenewicz, L.A., Huber, F.J., Bosurgi, L., Hu, B., Hedl, M., Zhang, W., O'Connor, W., Jr., Murphy, A.J., et al. (2012). IL-22BP is regulated by the inflammasome and modulates tumorigenesis in the intestine. Nature 491, 259–263. https://doi.org/10.1038/nature11535.

19. Perez, L.G., Kempski, J., McGee, H.M., Pelzcar, P., Agalioti, T., Giannou, A., Konczalla, L., Brockmann, L., Wahib, R., Xu, H., et al. (2020). TGF-beta signaling in Th17 cells promotes IL-22 production and colitis-associated colon cancer. Nat. Commun. 11, 2608. https://doi.org/10.1038/s41467-020-16363-w.

20. Meyer, A., Stark, M., Karstens, J.H., Christiansen, H., and Bruns, F. (2012). Langerhans cell histiocytosis of the cranial base: is low-dose radiotherapy effective? Case Rep. Oncol. Med. 2012, 789640. https://doi.org/10.1155/2012/789640.

21. Zhuang, Y., Peng, L.S., Zhao, Y.L., Shi, Y., Mao, X.H., Guo, G., Chen, W., Liu, X.F., Zhang, J.Y., Liu, T., et al. (2012). Increased intratumoral IL-22-producing CD4(+) T cells and Th22 cells correlate with gastric cancer progression and predict poor patient survival. Cancer Immunol. Immunother. 61, 1965–1975. https://doi.org/10.1007/s00262-012-1241-5.

22. Chen, X., Wang, Y., Wang, J., Wen, J., Jia, X., Wang, X., and Zhang, H. (2018). Accumulation of T-helper 22 cells, interleukin-22 and myeloid-derived suppressor cells promotes gastric cancer progression in elderly patients. Oncol. Lett. 16, 253–261. https://doi.org/10.3892/ol.2018.8612.

23. Doulabi, H., Rastin, M., Shabahangh, H., Maddah, G., Abdollahi, A., Nosratabadi, R., Esmaeili, S.A., and Mahmoudi, M. (2018). Analysis of Th22, Th17 and CD4(+)cells co-producing IL-17/IL-22 at different stages of human colon cancer. Biomed. Pharmacother. 103, 1101–1106. https://doi.org/10.1016/j.biopha.2018.04.147.

24. Zeng, H., Liu, Z., Wang, Z., Zhou, Q., Qi, Y., Chen, Y., Chen, L., Zhang, P., Wang, J., Chang, Y., et al. (2020). Intratumoral IL22-producing cells define immunoevasive subtype muscle-invasive bladder cancer with

poor prognosis and superior nivolumab responses. Int. J. Cancer *146*, 542–552. https://doi.org/10.1002/ijc.32715.

25. Jiang, R., Wang, H., Deng, L., Hou, J., Shi, R., Yao, M., Gao, Y., Yao, A., Wang, X., Yu, L., and Sun, B. (2013). IL-22 is related to development of human colon cancer by activation of STAT3. BMC Cancer *13*, 59. https://doi.org/10.1186/1471-2407-13-59.

26. Fukui, H., Zhang, X., Sun, C., Hara, K., Kikuchi, S., Yamasaki, T., Kondo, T., Tomita, T., Oshima, T., Watari, J., et al. (2014). IL-22 produced by cancer-associated fibroblasts promotes gastric cancer cell invasion via STAT3 and ERK signaling. Br. J. Cancer *111*, 763–771. https://doi.org/10.1038/bjc.2014.336.

27. Liu, T., Peng, L., Yu, P., Zhao, Y., Shi, Y., Mao, X., Chen, W., Cheng, P., Wang, T., Chen, N., et al. (2012). Increased circulating Th22 and Th17 cells are associated with tumor progression and patient survival in human gastric cancer. J. Clin. Immunol. *32*, 1332–1339. https://doi.org/10.1007/s10875-012-9718-8.

28. Niccolai, E., Taddei, A., Ricci, F., Rolla, S., D'Elios, M.M., Benagiano, M., Bechi, P., Bencini, L., Ringressi, M.N., Pini, A., et al. (2016). Intra-tumoral IFN-gamma-producing Th22 cells correlate with TNM staging and the worst outcomes in pancreatic cancer. Clin. Sci. *130*, 247–258. https://doi.org/10.1042/CS20150437.

29. Xu, X., Tang, Y., Guo, S., Zhang, Y., Tian, Y., Ni, B., and Wang, H. (2014). Increased intratumoral interleukin 22 levels and frequencies of interleukin 22-producing CD4+ T cells correlate with pancreatic cancer progression. Pancreas *43*, 470–477. https://doi.org/10.1097/MPA.0000000000000055.

30. Kotenko, S.V., Izotova, L.S., Mirochnitchenko, O.V., Esterova, E., Dickensheets, H., Donnelly, R.P., and Pestka, S. (2001). Identification of the functional interleukin-22 (IL-22) receptor complex: the IL-10R2 chain (IL-10Rbeta) is a common chain of both the IL-10 and IL-22 (IL-10-related T cell-derived inducible factor, IL-TIF) receptor complexes. J. Biol. Chem. *276*, 2725–2732. https://doi.org/10.1074/jbc.M007837200.

31. Ouyang, W., and O'Garra, A. (2019). IL-10 Family Cytokines IL-10 and IL-22: from Basic Science to Clinical Translation. Immunity *50*, 871–891. https://doi.org/10.1016/j.immuni.2019.03.020.

32. Kempski, J., Giannou, A.D., Riecken, K., Zhao, L., Steglich, B., Lücke, J., Garcia-Perez, L., Karstens, K.F., Wöstemeier, A., Nawrocki, M., et al. (2020). IL22BP Mediates the Antitumor Effects of Lymphotoxin Against Colorectal Tumors in Mice and Humans. Gastroenterology *159*, 1417–1430.e3. https://doi.org/10.1053/j.gastro.2020.06.033.

33. Kotenko, S.V., Izotova, L.S., Mirochnitchenko, O.V., Esterova, E., Dickensheets, H., Donnelly, R.P., and Pestka, S. (2001). Identification, cloning and characterization of a novel soluble receptor that binds IL-22 and neutralizes its activity. J. Immunol. *166*, 7096–7103. https://doi.org/10.4049/jimmunol.166.12.7096.

34. Dudakov, J.A., Hanash, A.M., and van den Brink, M.R.M. (2015). Interleukin-22: immunobiology and pathology. Annu. Rev. Immunol. *33*, 747–785. https://doi.org/10.1146/annurev-immunol-032414-112123.

35. Wolk, K., Kunz, S., Witte, E., Friedrich, M., Asadullah, K., and Sabat, R. (2004). IL-22 increases the innate immunity of tissues. Immunity *21*, 241–254. https://doi.org/10.1016/j.immuni.2004.07.007.

36. Sabat, R., Ouyang, W., and Wolk, K. (2014). Therapeutic opportunities of the IL-22-IL-22R1 system. Nat. Rev. Drug Discov. *13*, 21–38. https://doi.org/10.1038/nrd4176.

37. Zenewicz, L.A., Yancopoulos, G.D., Valenzuela, D.M., Murphy, A.J., Stevens, S., and Flavell, R.A. (2008). Innate and adaptive interleukin-22 protects mice from inflammatory bowel disease. Immunity *29*, 947–957. https://doi.org/10.1016/j.immuni.2008.11.003.

38. Gronke, K., Hernández, P.P., Zimmermann, J., Klose, C.S.N., Kofoed-Branzk, M., Guendel, F., Witkowski, M., Tizian, C., Amann, L., Schumacher, F., et al. (2019). Interleukin-22 protects intestinal stem cells against genotoxic stress. Nature *566*, 249–253. https://doi.org/10.1038/s41586-019-0899-7.

39. Saxton, R.A., Henneberg, L.T., Calafiore, M., Su, L., Jude, K.M., Hanash, A.M., and Garcia, K.C. (2021). The tissue protective functions of interleukin-22 can be decoupled from pro-inflammatory actions through structure-based design. Immunity *54*, 660–672.e9. https://doi.org/10.1016/j.immuni.2021.03.008.

40. Dumoutier, L., Louahed, J., and Renauld, J.C. (2000). Cloning and characterization of IL-10-related T cell-derived inducible factor (IL-TIF), a novel cytokine structurally related to IL-10 and inducible by IL-9. J. Immunol. *164*, 1814–1819. https://doi.org/10.4049/jimmunol.164.4.1814.

41. Lejeune, D., Dumoutier, L., Constantinescu, S., Kruijer, W., Schuringa, J.J., and Renauld, J.C. (2002). Interleukin-22 (IL-22) activates the JAK/STAT, ERK, JNK, and p38 MAP kinase pathways in a rat hepatoma cell line. Pathways that are shared with and distinct from IL-10. J. Biol. Chem. *277*, 33676–33682. https://doi.org/10.1074/jbc.M204204200.

42. Nagalakshmi, M.L., Rascle, A., Zurawski, S., Menon, S., and de Waal Malefyt, R. (2004). Interleukin-22 activates STAT3 and induces IL-10 by colon epithelial cells. Int. Immunopharmacol. *4*, 679–691. https://doi.org/10.1016/j.intimp.2004.01.008.

43. Mitra, A., Raychaudhuri, S.K., and Raychaudhuri, S.P. (2012). IL-22 induced cell proliferation is regulated by PI3K/Akt/mTOR signaling cascade. Cytokine *60*, 38–42. https://doi.org/10.1016/j.cyto.2012.06.316.

44. Bachmann, M., Ulziibat, S., Härdle, L., Pfeilschifter, J., and Mühl, H. (2013). IFNalpha converts IL-22 into a cytokine efficiently activating STAT1 and its downstream targets. Biochem. Pharmacol. *85*, 396–403. https://doi.org/10.1016/j.bcp.2012.11.004.

45. Zheng, Y., Valdez, P.A., Danilenko, D.M., Hu, Y., Sa, S.M., Gong, Q., Abbas, A.R., Modrusan, Z., Ghilardi, N., de Sauvage, F.J., and Ouyang, W. (2008). Interleukin-22 mediates early host defense against attaching and effacing bacterial pathogens. Nat. Med. *14*, 282–289. https://doi.org/10.1038/nm1720.

46. Andoh, A., Zhang, Z., Inatomi, O., Fujino, S., Deguchi, Y., Araki, Y., Tsujikawa, T., Kitoh, K., Kim-Mitsuyama, S., Takayanagi, A., et al. (2005). Interleukin-22, a member of the IL-10 subfamily, induces inflammatory responses in colonic subepithelial myofibroblasts. Gastroenterology *129*, 969–984. https://doi.org/10.1053/j.gastro.2005.06.071.

47. Tufman, A., Huber, R.M., Völk, S., Aigner, F., Edelmann, M., Gamarra, F., Kiefl, R., Kahnert, K., Tian, F., Boulesteix, A.L., et al. (2016). Interleukin-22 is elevated in lavage from patients with lung cancer and other pulmonary diseases. BMC Cancer *16*, 409. https://doi.org/10.1186/s12885-016-2471-2.

48. Voigt, C., May, P., Gottschlich, A., Markota, A., Wenk, D., Gerlach, I., Voigt, S., Stathopoulos, G.T., Arendt, K.A.M., Heise, C., et al. (2017). Cancer cells induce interleukin-22 production from memory CD4(+) T cells via interleukin-1 to promote tumor growth. Proc. Natl. Acad. Sci. USA *114*, 12994–12999. https://doi.org/10.1073/pnas.1705165114.

49. Markota, A., Endres, S., and Kobold, S. (2018). Targeting interleukin-22 for cancer therapy. Hum. Vaccin. Immunother. *14*, 2012–2015. https://doi.org/10.1080/21645515.2018.1461300.

50. Ewens, A., Mihich, E., and Ehrke, M.J. (2005). Distant metastasis from subcutaneously grown E0771 medullary breast adenocarcinoma. Anticancer Res. *25*, 3905–3915.

51. Sugiura, K., and Stock, C.C. (1952). Studies in a tumor spectrum. I. Comparison of the action of methylbis (2-chloroethyl)amine and 3-bis(2-chloroethyl)aminomethyl-4-methoxymethyl -5-hydroxy-6-methylpyridine on the growth of a variety of mouse and rat tumors. Cancer *5*, 382–402. https://doi.org/10.1002/1097-0142(195203)5:2<382::aid-cncr2820050229>3.0.co;2-3.

52. Renier, N., Wu, Z., Simon, D.J., Yang, J., Ariel, P., and Tessier-Lavigne, M. (2014). iDISCO: a simple, rapid method to immunolabel large tissue samples for volume imaging. Cell *159*, 896–910. https://doi.org/10.1016/j.cell.2014.10.010.

53. Kleinschmidt, D., Giannou, A.D., McGee, H.M., Kempski, J., Steglich, B., Huber, F.J., Ernst, T.M., Shiri, A.M., Wegscheid, C., Tasika, E., et al.

(2017). A protective function of IL-22BP in ischemia reperfusion and acetaminophen-induced liver injury. J. Immunol. *199*, 4078–4090. https://doi.org/10.4049/jimmunol.1700587.

54. O'Donnell, J.S., Madore, J., Li, X.Y., and Smyth, M.J. (2020). Tumor intrinsic and extrinsic immune functions of CD155. Semin. Cancer Biol. *65*, 189–196. https://doi.org/10.1016/j.semcancer.2019.11.013.

55. Molfetta, R., Zitti, B., Lecce, M., Milito, N.D., Stabile, H., Fionda, C., Cippitelli, M., Gismondi, A., Santoni, A., and Paolini, R. (2020). CD155: a multi-functional molecule in tumor progression. Int. J. Mol. Sci. *21*, 922. https://doi.org/10.3390/ijms21030922.

56. Gao, J., Zheng, Q., Xin, N., Wang, W., and Zhao, C. (2017). CD155, an onco-immunologic molecule in human tumors. Cancer Sci. *108*, 1934–1938. https://doi.org/10.1111/cas.13324.

57. Morimoto, K., Satoh-Yamaguchi, K., Hamaguchi, A., Inoue, Y., Takeuchi, M., Okada, M., Ikeda, W., Takai, Y., and Imai, T. (2008). Interaction of cancer cells with platelets mediated by Necl-5/poliovirus receptor enhances cancer cell metastasis to the lungs. Oncogene *27*, 264–273. https://doi.org/10.1038/sj.onc.1210645.

58. Chan, C.J., Martinet, L., Gilfillan, S., Souza-Fonseca-Guimaraes, F., Chow, M.T., Town, L., Ritchie, D.S., Colonna, M., Andrews, D.M., and Smyth, M.J. (2014). The receptors CD96 and CD226 oppose each other in the regulation of natural killer cell functions. Nat. Immunol. *15*, 431–438. https://doi.org/10.1038/ni.2850.

59. Fuchs, A., Cella, M., Giurisato, E., Shaw, A.S., and Colonna, M. (2004). Cutting edge: CD96 (tactile) promotes NK cell-target cell adhesion by interacting with the poliovirus receptor (CD155). J. Immunol. *172*, 3994–3998. https://doi.org/10.4049/jimmunol.172.7.3994.

60. Jarosch, S., Köhlen, J., Wagner, S., D'Ippolito, E., and Busch, D.H. (2022). ChipCytometry for multiplexed detection of protein and mRNA markers on human FFPE tissue samples. STAR Protoc. *3*, 101374. https://doi.org/10.1016/j.xpro.2022.101374.

61. Chauvin, J.M., Ka, M., Pagliano, O., Menna, C., Ding, Q., DeBlasio, R., Sanders, C., Hou, J., Li, X.Y., Ferrone, S., et al. (2020). IL15 stimulation with TIGIT blockade reverses CD155-mediated NK-Cell dysfunction in melanoma. Clin. Cancer Res. *26*, 5520–5533. https://doi.org/10.1158/1078-0432.CCR-20-0575.

62. Weulersse, M., Asrir, A., Pichler, A.C., Lemaitre, L., Braun, M., Carrié, N., Joubert, M.V., Le Moine, M., Do Souto, L., Gaud, G., et al. (2020). Eomes-dependent loss of the co-activating receptor CD226 restrains CD8(+) T cell anti-tumor functions and limits the efficacy of cancer immunotherapy. Immunity *53*, 824–839.e10. https://doi.org/10.1016/j.immuni.2020.09.006.

63. Braun, M., Aguilera, A.R., Sundarrajan, A., Corvino, D., Stannard, K., Krumeich, S., Das, I., Lima, L.G., Meza Guzman, L.G., Li, K., et al. (2020). CD155 on tumor cells drives resistance to immunotherapy by inducing the degradation of the activating receptor CD226 in CD8(+) T cells. Immunity *53*, 805–823.e15. https://doi.org/10.1016/j.immuni.2020.09.010.

64. Lepletier, A., Madore, J., O'Donnell, J.S., Johnston, R.L., Li, X.Y., McDonald, E., Ahern, E., Kuchel, A., Eastgate, M., Pearson, S.A., et al. (2020). Tumor CD155 expression is associated with resistance to anti-PD1 immunotherapy in metastatic melanoma. Clin. Cancer Res. *26*, 3671–3681. https://doi.org/10.1158/1078-0432.CCR-19-3925.

65. Newman, A.M., Steen, C.B., Liu, C.L., Gentles, A.J., Chaudhuri, A.A., Scherer, F., Khodadoust, M.S., Esfahani, M.S., Luca, B.A., Steiner, D., et al. (2019). Determining cell type abundance and expression from bulk tissues with digital cytometry. Nat. Biotechnol. *37*, 773–782. https://doi.org/10.1038/s41587-019-0114-2.

66. Soriani, A., Zingoni, A., Cerboni, C., Iannitto, M.L., Ricciardi, M.R., Di Gialleonardo, V., Cippitelli, M., Fionda, C., Petrucci, M.T., Guarini, A., et al. (2009). ATM-ATR-dependent up-regulation of DNAM-1 and NKG2D ligands on multiple myeloma cells by therapeutic agents results in enhanced NK-cell susceptibility and is associated with a senescent phenotype. Blood *113*, 3503–3511. https://doi.org/10.1182/blood-2008-08-173914.

67. Fionda, C., Abruzzese, M.P., Zingoni, A., Soriani, A., Ricci, B., Molfetta, R., Paolini, R., Santoni, A., and Cippitelli, M. (2015). Nitric oxide donors increase PVR/CD155 DNAM-1 ligand expression in multiple myeloma cells: role of DNA damage response activation. BMC Cancer *15*, 17. https://doi.org/10.1186/s12885-015-1023-5.

68. Ardolino, M., Zingoni, A., Cerboni, C., Cecere, F., Soriani, A., Iannitto, M.L., and Santoni, A. (2011). DNAM-1 ligand expression on Ag-stimulated T lymphocytes is mediated by ROS-dependent activation of DNA-damage response: relevance for NK-T cell interaction. Blood *117*, 4778–4786. https://doi.org/10.1182/blood-2010-08-300954.

69. Refae, S., Gal, J., Brest, P., Giacchero, D., Borchiellini, D., Ebran, N., Peyrade, F., Guigay, J., Milano, G., and Saada-Bouzid, E. (2020). Hyperprogression under Immune Checkpoint Inhibitor: a potential role for germinal immunogenetics. Sci. Rep. *10*, 3565. https://doi.org/10.1038/s41598-020-60437-0.

70. Westendorf, K., Durek, P., Ayew, S., Mashreghi, M.F., and Radbruch, A. (2016). Chromosomal localisation of the CD4cre transgene in B6.Cg-Tg(Cd4-cre)1Cwi mice. J. Immunol. Methods *436*, 54–57. https://doi.org/10.1016/j.jim.2016.06.005.

71. St Paul, M., Saibil, S.D., Lien, S.C., Han, S., Sayad, A., Mulder, D.T., Garcia-Batres, C.R., Elford, A.R., Israni-Winger, K., Robert-Tissot, C., et al. (2020). IL6 Induces an IL22(+) CD8(+) T-cell Subset with Potent Antitumor Function. Cancer Immunol. Res. *8*, 321–333. https://doi.org/10.1158/2326-6066.CIR-19-0521.

72. St Paul, M., Saibil, S.D., Han, S., Israni-Winger, K., Lien, S.C., Laister, R.C., Sayad, A., Penny, S., Amaria, R.N., Haydu, L.E., et al. (2021). Coenzyme A fuels T cell anti-tumor immunity. Cell Metab. *33*, 2415–2427.e6. https://doi.org/10.1016/j.cmet.2021.11.010.

73. Jin, C., Lagoudas, G.K., Zhao, C., Bullman, S., Bhutkar, A., Hu, B., Ameh, S., Sandel, D., Liang, X.S., Mazzilli, S., et al. (2019). Commensal microbiota promote lung cancer development via gammadelta T cells. Cell *176*, 998–1013.e16. https://doi.org/10.1016/j.cell.2018.12.040.

74. Bi, Y., Cao, J., Jin, S., Lv, L., Qi, L., Liu, F., Geng, J., and Yu, Y. (2016). Interleukin-22 promotes lung cancer cell proliferation and migration via the IL-22R1/STAT3 and IL-22R1/AKT signaling pathways. Mol. Cell. Biochem. *415*, 1–11. https://doi.org/10.1007/s11010-016-2663-8.

75. Wen, Z., Liao, Q., Zhao, J., Hu, Y., You, L., Lu, Z., Jia, C., Wei, Y., and Zhao, Y. (2014). High expression of interleukin-22 and its receptor predicts poor prognosis in pancreatic ductal adenocarcinoma. Ann. Surg. Oncol. *21*, 125–132. https://doi.org/10.1245/s10434-013-3322-x.

76. Lim, C., and Savan, R. (2014). The role of the IL-22/IL-22R1 axis in cancer. Cytokine Growth Factor Rev. *25*, 257–271. https://doi.org/10.1016/j.cytogfr.2014.04.005.

77. Perusina Lanfranca, M., Zhang, Y., Girgis, A., Kasselman, S., Lazarus, J., Kryczek, I., Delrosario, L., Rhim, A., Koneva, L., Sartor, M., et al. (2020). Interleukin 22 signaling regulates acinar cell plasticity to promote pancreatic tumor development in mice. Gastroenterology *158*, 1417–1432.e11. https://doi.org/10.1053/j.gastro.2019.12.010.

78. Giannou A.D., Kempski J., Shiri A.M., Lücke J., Zhang T., Zhao L., Zazara D.E., Cortesi, F., Riecken, K., Amezcua Vesely, M.C., et al. Tissue resident iNKT17 cells facilitate cancer cell extravasation in liver metastasis via Interleukin-22. Immunity. 2023;56.

79. Zhuo, B., Li, Y., Gu, F., Li, Z., Sun, Q., Shi, Y., Shen, Y., Zhang, F., Wang, R., and Wang, X. (2018). Overexpression of CD155 relates to metastasis and invasion in osteosarcoma. Oncol. Lett. *15*, 7312–7318. https://doi.org/10.3892/ol.2018.8228.

80. Iguchi-Manaka, A., Okumura, G., Ichioka, E., Kiyomatsu, H., Ikeda, T., Bando, H., Shibuya, A., and Shibuya, K. (2020). High expression of soluble CD155 in estrogen receptor-negative breast cancer. Breast cancer *27*, 92–99. https://doi.org/10.1007/s12282-019-00999-8.

81. Triki, H., Charfi, S., Bouzidi, L., Ben Kridis, W., Daoud, J., Chaabane, K., Sellami-Boudawara, T., Rebai, A., and Cherif, B. (2019). CD155 expression in human breast cancer: clinical significance and relevance to natural killer cell infiltration. Life Sci. *231*, 116543. https://doi.org/10.1016/j.lfs.2019.116543.

82. Xu, Y., Cui, G., Jiang, Z., Li, N., and Zhang, X. (2019). Survival analysis with regard to PD-L1 and CD155 expression in human small cell lung cancer and a comparison with associated receptors. Oncol. Lett. *17*, 2960–2968. https://doi.org/10.3892/ol.2019.9910.

83. Yong, H., Cheng, R., Li, X., Gao, G., Jiang, X., Cheng, H., Zhou, X., and Zhao, W. (2019). CD155 expression and its prognostic value in postoperative patients with breast cancer. Biomed. Pharmacother. *115*, 108884. https://doi.org/10.1016/j.biopha.2019.108884.

84. Zheng, Q., Gao, J., Yin, P., Wang, W., Wang, B., Li, Y., and Zhao, C. (2020). CD155 contributes to the mesenchymal phenotype of triple-negative breast cancer. Cancer Sci. *111*, 383–394. https://doi.org/10.1111/cas.14276.

85. Kučan Brlić, P., Lenac Roviš, T., Cinamon, G., Tsukerman, P., Mandelboim, O., and Jonjić, S. (2019). Targeting PVR (CD155) and its receptors in anti-tumor therapy. Cell. Mol. Immunol. *16*, 40–52. https://doi.org/10.1038/s41423-018-0168-y.

86. Blake, S.J., Stannard, K., Liu, J., Allen, S., Yong, M.C.R., Mittal, D., Aguilera, A.R., Miles, J.J., Lutzky, V.P., de Andrade, L.F., et al. (2016). Suppression of Metastases Using a New Lymphocyte Checkpoint Target for Cancer Immunotherapy. Cancer Discov. *6*, 446–459. https://doi.org/10.1158/2159-8290.CD-15-0944.

87. Chan, C.J., Andrews, D.M., McLaughlin, N.M., Yagita, H., Gilfillan, S., Colonna, M., and Smyth, M.J. (2010). DNAM-1/CD155 interactions promote cytokine and NK cell-mediated suppression of poorly immunogenic melanoma metastases. J. Immunol. *184*, 902–911. https://doi.org/10.4049/jimmunol.0903225.

88. Jin, H.S., Ko, M., Choi, D.S., Kim, J.H., Lee, D.H., Kang, S.H., Kim, I., Lee, H.J., Choi, E.K., Kim, K.P., et al. (2020). CD226(hi)CD8(+) T Cells Are a Prerequisite for Anti-TIGIT Immunotherapy. Cancer Immunol. Res. *8*, 912–925. https://doi.org/10.1158/2326-6066.CIR-19-0877.

89. Guillon, A., Gueugnon, F., Mavridis, K., Dalloneau, E., Jouan, Y., Diot, P., Heuzé-Vourc'h, N., Courty, Y., and Si-Tahar, M. (2016). Interleukin-22 receptor is overexpressed in nonsmall cell lung cancer and portends a poor prognosis. Eur. Respir. J. *47*, 1277–1280. https://doi.org/10.1183/13993003.01580-2015.

90. He, W., Wu, J., Shi, J., Huo, Y.M., Dai, W., Geng, J., Lu, P., Yang, M.W., Fang, Y., Wang, W., et al. (2018). IL22RA1/STAT3 signaling promotes stemness and tumorigenicity in pancreatic cancer. Cancer Res. *78*, 3293–3305. https://doi.org/10.1158/0008-5472.CAN-17-3131.

91. Waidmann, O., Kronenberger, B., Scheiermann, P., Köberle, V., Mühl, H., and Piiper, A. (2014). Interleukin-22 serum levels are a negative prognostic indicator in patients with hepatocellular carcinoma. Hepatology *59*, 1207. https://doi.org/10.1002/hep.26528.

92. Bruni, D., Angell, H.K., and Galon, J. (2020). The immune contexture and Immunoscore in cancer prognosis and therapeutic efficacy. Nat. Rev. Cancer *20*, 662–680. https://doi.org/10.1038/s41568-020-0285-7.

93. Banta, K.L., Xu, X., Chitre, A.S., Au-Yeung, A., Takahashi, C., O'Gorman, W.E., Wu, T.D., Mittman, S., Cubas, R., Comps-Agrar, L., et al. (2022). Mechanistic convergence of the TIGIT and PD-1 inhibitory pathways necessitates co-blockade to optimize anti-tumor CD8(+) T cell responses. Immunity *55*, 512–526.e9. https://doi.org/10.1016/j.immuni.2022.02.005.

94. Bi, J. (2022). CD226: a potent driver of antitumor immunity that needs to be maintained. Cell. Mol. Immunol. *19*, 969–970. https://doi.org/10.1038/s41423-020-00633-0.

95. Guttman-Yassky, E., Brunner, P.M., Neumann, A.U., Khattri, S., Pavel, A.B., Malik, K., Singer, G.K., Baum, D., Gilleaudeau, P., Sullivan-Whalen, M., et al. (2018). Efficacy and safety of fezakinumab (an IL-22 monoclonal antibody) in adults with moderate-to-severe atopic dermatitis inadequately controlled by conventional treatments: A randomized, double-blind, phase 2a trial. J. Am. Acad. Dermatol. *78*, 872–881.e6. https://doi.org/10.1016/j.jaad.2018.01.016.

96. Hotta, A., Cheung, A.Y.L., Farra, N., Vijayaragavan, K., Séguin, C.A., Draper, J.S., Pasceri, P., Maksakova, I.A., Mager, D.L., Rossant, J., et al. (2009). Isolation of human iPS cells using EOS lentiviral vectors to select for pluripotency. Nat. Methods *6*, 370–376. https://doi.org/10.1038/nmeth.1325.

97. Ran, F.A., Hsu, P.D., Lin, C.Y., Gootenberg, J.S., Konermann, S., Trevino, A.E., Scott, D.A., Inoue, A., Matoba, S., Zhang, Y., and Zhang, F. (2013). Double nicking by RNA-guided CRISPR Cas9 for enhanced genome editing specificity. Cell *154*, 1380–1389. https://doi.org/10.1016/j.cell.2013.08.021.

98. Slaymaker, I.M., Gao, L., Zetsche, B., Scott, D.A., Yan, W.X., and Zhang, F. (2016). Rationally engineered Cas9 nucleases with improved specificity. Science *351*, 84–88. https://doi.org/10.1126/science.aad5227.

99. Stewart, S.A., Dykxhoorn, D.M., Palliser, D., Mizuno, H., Yu, E.Y., An, D.S., Sabatini, D.M., Chen, I.S.Y., Hahn, W.C., Sharp, P.A., et al. (2003). Lentivirus-delivered stable gene silencing by RNAi in primary cells. RNA *9*, 493–501. https://doi.org/10.1261/rna.2192803.

100. Labun, K., Montague, T.G., Krause, M., Torres Cleuren, Y.N., Tjeldnes, H., and Valen, E. (2019). CHOPCHOP v3: expanding the CRISPR web toolbox beyond genome editing. Nucleic Acids Res. *47*, W171–W174. https://doi.org/10.1093/nar/gkz365.

101. Perez, F., and Granger, B.E. (2007). IPython: A System for Interactive Scientific Computing. Comput. Sci. Eng. *9*, 21–29. https://doi.org/10.1109/mcse.2007.53.

102. Kluyver, T., Ragan-Kelley, B., Pérez, F., Granger, B., Bussonnier, M., Frederic, J., Kelley, K., Hamrick, J., Grout, J., Corlay, S., et al. (2016). Jupyter Notebooks – a publishing format for reproducible computational workflows. In 20th International Conference on Electronic Publishing (01/01/16), F. Loizides and B. Scmidt, eds. (IOS Press).

103. Harris, C.R., Millman, K.J., van der Walt, S.J., Gommers, R., Virtanen, P., Cournapeau, D., Wieser, E., Taylor, J., Berg, S., Smith, N.J., et al. (2020). Array programming with NumPy. Nature *585*, 357–362. https://doi.org/10.1038/s41586-020-2649-2.

104. Reback, J., jbrockmendel, McKinney, W., Van den Bossche, J., Augspurger, T., Roeschke, M., Hawkins, S., and Cloud, P.; gfyoung; Sinhrks (2020). pandas-dev/pandas: Pandas 1.4.2.

105. McKinney, W. (2010). Data Structures for Statistical Computing in Python. https://doi.org/10.25080/Majora-92bf1922-00a.

106. Developers, T.F. (2022). TensorFlow.

107. Pedregosa, F., Varoquaux, G., Gramfort, A., Michel, V., Thirion, B., Grisel, O., Blondel, M., Prettenhofer, P., Weiss, R., Dubourg, V., et al. (2011). Scikit-learn: Machine Learning in Python. J. Mach. Learn. Res. *12*, 2825–2830.

108. Hunter, J.D. (2007). Matplotlib: A 2D Graphics Environment. Comput. Sci. Eng. *9*, 90–95. https://doi.org/10.1109/MCSE.2007.55.

109. Waskom, M. (2021). seaborn: statistical data visualization. J. Open Source Softw. *6*, 3021. https://doi.org/10.21105/joss.03021.

110. Virtanen, P., Gommers, R., Oliphant, T.E., Haberland, M., Reddy, T., Cournapeau, D., Burovski, E., Peterson, P., Weckesser, W., Bright, J., et al. (2020). SciPy 1.0: fundamental algorithms for scientific computing in Python. Nat. Methods *17*, 261–272. https://doi.org/10.1038/s41592-019-0686-2.

111. Davidson-Pilon, C. (2019). Lifelines: survival analysis in Python. J. Open Source Softw. *4*, 1317. https://doi.org/10.21105/joss.01317.

112. Gazoni, E., and Clark, C. (2021). openpyxl - A Python Library to Read/write Excel 2010 xlsx/xlsm files.

113. Schindelin, J., Arganda-Carreras, I., Frise, E., Kaynig, V., Longair, M., Pietzsch, T., Preibisch, S., Rueden, C., Saalfeld, S., Schmid, B., et al. (2012). Fiji: an open-source platform for biological-image analysis. Nat. Methods *9*, 676–682. https://doi.org/10.1038/nmeth.2019.

114. Jarosch, S., Köhlen, J., Sarker, R.S.J., Steiger, K., Janssen, K.-P., Christians, A., Hennig, C., Holler, E., D'Ippolito, E., and Busch, D.H. (2021). Multiplexed imaging and automated signal quantification in formalin-fixed paraffin-embedded tissues by ChipCytometry. Cell Rep. Methods *1*, 100104. https://doi.org/10.1016/j.crmeth.2021.100104.

115. Preibisch, S., Saalfeld, S., and Tomancak, P. (2009). Globally optimal stitching of tiled 3D microscopic image acquisitions. Bioinformatics *25*, 1463–1465. https://doi.org/10.1093/bioinformatics/btp184.

116. Peng, T., Thorn, K., Schroeder, T., Wang, L., Theis, F.J., Marr, C., and Navab, N. (2017). A BaSiC tool for background and shading correction of optical microscopy images. Nat. Commun. *8*, 14836. https://doi.org/10.1038/ncomms14836.

117. Schmidt, U., Weigert, M., Broaddus, C., and Myers, G. (2018). Cell Detection with Star-convex Polygons. Medical Image Computing and Computer Assisted Intervention MICCAI 2018 (Springer International Publishing).

118. Tang, T., Li, L., Tang, J., Li, Y., Lin, W.Y., Martin, F., Grant, D., Solloway, M., Parker, L., Ye, W., et al. (2010). A mouse knockout library for secreted and transmembrane proteins. Nat. Biotechnol. *28*, 749–755. https://doi.org/10.1038/nbt.1644.

119. Esplugues, E., Huber, S., Gagliani, N., Hauser, A.E., Town, T., Wan, Y.Y., O'Connor, W., Jr., Rongvaux, A., Van Rooijen, N., Haberman, A.M., et al. (2011). Control of TH17 cells occurs in the small intestine. Nature *475*, 514–518. https://doi.org/10.1038/nature10228.

120. Wan, Y.Y., and Flavell, R.A. (2005). Identifying Foxp3-expressing suppressor T cells with a bicistronic reporter. Proc. Natl. Acad. Sci. USA *102*, 5126–5131. https://doi.org/10.1073/pnas.0501701102.

121. Giannou, A.D., Marazioti, A., Kanellakis, N.I., Giopanou, I., Lilis, I., Zazara, D.E., Ntaliarda, G., Kati, D., Armenis, V., Giotopoulou, G.A., et al. (2017). NRAS destines tumor cells to the lungs. EMBO Mol. Med. *9*, 672–686. https://doi.org/10.15252/emmm.201606978.

122. Soares, K.C., Foley, K., Olino, K., Leubner, A., Mayo, S.C., Jain, A., Jaffee, E., Schulick, R.D., Yoshimura, K., Edil, B., and Zheng, L. (2014). A preclinical murine model of hepatic metastases. JoVE *51677*, 51677. https://doi.org/10.3791/51677.

123. Aslakson, C.J., and Miller, F.R. (1992). Selective events in the metastatic process defined by analysis of the sequential dissemination of subpopulations of a mouse mammary tumor. Cancer Res. *52*, 1399–1405.

124. Heckman, K.L., and Pease, L.R. (2007). Gene splicing and mutagenesis by PCR-driven overlap extension. Nat. Protoc. *2*, 924–932. https://doi.org/10.1038/nprot.2007.132.

125. Emgård, J., Kammoun, H., García-Cassani, B., Chesné, J., Parigi, S.M., Jacob, J.M., Cheng, H.W., Evren, E., Das, S., Czarnewski, P., et al. (2018). Oxysterol sensing through the receptor GPR183 promotes the lymphoid-tissue-inducing function of innate lymphoid cells and colonic inflammation. Immunity *48*, 120–132.e8. https://doi.org/10.1016/j.immuni.2017.11.020.

126. Hoffmann, F.M., Berger, J.L., Lingel, I., Laumonnier, Y., Lewkowich, I.P., Schmudde, I., and König, P. (2018). Distribution and interaction of murine pulmonary phagocytes in the naive and allergic lung. Front. Immunol. *9*, 1046. https://doi.org/10.3389/fimmu.2018.01046.

127. Gan, Y., Li, N., Zou, G., Xin, Y., and Guan, J. (2018). Identification of cancer subtypes from single-cell RNA-seq data using a consensus clustering method. BMC Med. Genomics *11*, 117. https://doi.org/10.1186/s12920-018-0433-z.

128. Chen, B., Khodadoust, M.S., Liu, C.L., Newman, A.M., and Alizadeh, A.A. (2018). Profiling tumor infiltrating immune cells with CIBERSORT. Methods Mol. Biol. *1711*, 243–259. https://doi.org/10.1007/978-1-4939-7493-1_12.

STAR★METHODS

KEY RESOURCES TABLE

REAGENT or RESOURCE	SOURCE	IDENTIFIER
Antibodies		
Anti-mouse TruStain fcX (CD16/32)	Biolegend	Cat# 101320; RRID:AB_1574975
Anti-mouse CD45 (30-F11) BV510	Biolegend	Cat# 103137; RRID:AB_2561392
Anti-mouse CD45 (I3/2.3) AF700	Biolegend	Cat# 147716; RRID:AB_2750449
Anti-mouse CD3e(145-2C11) BV605	Biolegend	Cat# 100302; RRID:AB_312667
Anti-mouse CD3e (17A2) BV650	Biolegend	Cat# 100229; RRID:AB_11204249
Anti-mouse CD3e (17A2) Pacific Blue	Biolegend	Cat# 100213; RRID:AB_493644
Anti-mouse CD3e (17A2) AF700	Biolegend	Cat# 100216; RRID:AB_493697
Anti-mouse CD3e (17A2) PE	Biolegend	Cat# 100206; RRID:AB_312663
Anti-mouse CD4 (GK1.5) BV786	Biolegend	Cat# 100453; RRID:AB_2565843
Anti-mouse CD4 (GK1.5) AF700	Biolegend	Cat# 100429; RRID:AB_493698
Anti-mouse CD4 (GK1.5) Pacific Blue	Biolegend	Cat# 100428; RRID:AB_493647
Anti-mouse CD4 (GK1.5) APC-Cy7	Biolegend	Cat# 100413; RRID:AB_312698
Anti-mouse CD4 (RM4-5) PerCP/Cy5.5	Biolegend	Cat# 100539; RRID:AB_893332
Anti-mouse CD8a (53-6.7) AF700	Biolegend	Cat# 100730; RRID:AB_493703
Anti-mouse CD8a (53-6.7) PerCP-Cy5.5	Biolegend	Cat# 100733; RRID:AB_2075239
Anti-mouse CD8a (53-6.7) Alexa Fluor 647	Biolegend	Cat# 100724; RRID:AB_389326
Anti-mouse CD8a (53-6.7) PE-Cy7	Biolegend	Cat# 100722; RRID:AB_312761
Anti-mouse CD8 (EPR21769) Alexa Fluor 555	abcam	Cat# 280863; RRID:AB_2927548
Anti-mouse $\gamma\delta$TCR (GL3) PerCP-Cy5.5	Biolegend	Cat# 118118; RRID:AB_10612756
Anti-mouse $\gamma\delta$TCR (UC7-13D5) PE	Biolegend	Cat# 107508; RRID:AB_345266
Anti-mouse CD49b (Hma2) PE	Biolegend	Cat# 103506; RRID:AB_313029
Anti-mouse CD49b (DX5) FITC	Biolegend	Cat# 108905; RRID:AB_313412
Anti-mouse NK-1.1 (PK136) PE-Cy7	Biolegend	Cat# 108714; RRID:AB_389364
Anti-mouse NKp46 (polyclonal)	R&D	Cat# AF2225; RRID:AB_355192
Anti-mouse CD127 (A7R34) BV421	Biolegend	Cat# 135027; RRID:AB_2563103
Anti-mouse CD155 (PVR, 4.24.1) PE	Biolegend	Cat# 132206; RRID:AB_1279103
Anti-mouse CD155 (polyclonal)	abcam	Cat# 230338; RRID:AB_2927547
Anti-mouse CD226 (TX42.1) BV711	Biolegend	Cat# 133609; RRID:AB_2715922
Anti-mouse TIGIT (1G9) APC	Biolegend	Cat# 142105; RRID:AB_10960139
Anti-mouse CD96 (3.3) PE	Biolegend	Cat# 131705; RRID:AB_1279389
Anti-mouse/human CD44 (IM7) Alexa Fluor 700	Biolegend	Cat# 103026; RRID:AB_493713
Anti-mouse IL-22 (IL-22JOP) APC	eBioscience (ThermoFisher)	Cat# 17-7222-82; RRID:AB_10597583
Anti-mouse IFN-γ (XMG1.2) PE-Cy7	eBioscience (ThermoFisher)	Cat# 25-7311-82; RRID:AB_469680
Fluorescein (FITC) AffiniPure Donkey Anti-Goat IgG (H + L)	Jackson ImmunoResearch	Cat# 705-095-003; RRID:AB_2340400
Ultra-LEAF™ Purified anti-mouse CD226 (DNAM-1) Antibody (480.1)	Biolegend	Cat# 132010; RRID: AB_2876467
InVivoMAb rat IgG2a (RG7/1.30)	BioXcell	Cat# BE0251; RRID: AB_2687732
InVivoMAb anti-mouse TIGIT (1G9)	BioXCell	Cat# BE0274; RRID:AB_2687797
InVivoMAb anti-mouse CD96 (3.3)	BioXCell	Cat# BE0337; RRID: AB_2894757
InVivoMAb rat IgG1 isotype control	BioXcell	Cat# BE0088; RRID:AB_1107775
Bacterial and virus strains		
5-alpha Competent *E. coli* (DH5α)	NEB	Cat# C2987U

(Continued on next page)

Continued

REAGENT or RESOURCE	SOURCE	IDENTIFIER
Chemicals, peptides, and recombinant proteins		
2-hydroxyethyl agarose (Agarose VII)	Sigma-Aldrich	Cat# A0701-100G
Biozym Sieve GeneticPure Agarose	Biozym	Cat# 850080
6-Thioguanine nucleotide	Sigma-Aldrich	Cat# A4882-500MG
Crystal violet dust	Sigma-Aldrich	Cat# C0775-100G
BD Pharm lyse buffer (10x)	BD Biosciences	Cat# 555899
Colagenase type I	Sigma-Aldrich	Cat# C0130-500MG
CountBright Plus Absolute Counting Beads	ThermoFischer	Cat# C36995
Percoll	GE Healthcare (Cytiva)	Cat# 17-0891-01
GolgiPlug (Brefeldin A)	BD Biosciences	Cat# 555029
GolgiStop (Monensin)	BD Biosciences	Cat# 554724
Ionomycin calcium salt	Sigma-Aldrich	Cat# I0634-5MG
PMA (phorbol 12-myristate 13-acetate)	Sigma-Aldrich	Cat# P1585-10MG
Red Blood Cell Lysis Buffer	Sigma-Aldrich	Cat# 11814389001
Dibenzyl ether	Sigma-Aldrich	Cat# 108014
DNase I	Sigma-Aldrich	Cat# 10104159001
EcoRI	NEB	Cat# R0101S
Xhoa-I	NEB	Cat# R0146L
Lipofectamine 2000 transfection reagent	ThermoFischer	Cat# 11668030
Polybrene	Sigma-Aldrich	Cat# TR-1003-G
G418, Geneticin	Sigma-Aldrich	Cat# 4727878001
NTB (nitroblue tetrazolium chloride)	ThermoFisher	Cat# N6495
Recombinant IL-22 (murine)	PeproTech	Cat# 210-22
D-Luciferin potassium salt	Perkin Elmer, USA	Cat# 122799
Hoechst 33,342	ThermoFisher	Cat# H1399
Fixable Viability Dye, eFluor® 780	ThermoFisher	Cat# 65-0865-14
Pacific Orange™ Succinimidyl Ester, Triethylammonium Salt	ThermoFisher	Cat# P30253
NucRed Live 647 ReadyProbes Reagent	ThermoFisher	Cat# R37106
Pro-Long Glass Antifade Mountant	ThermoFisher	Cat# P36984
Pro-Long Live Antifade Reagent	ThermoFisher	Cat# P369745
Normal Donkey Serum, IgG	Biozol	SBA-0030-01
Normal Rabbit Serum, IgG	Biozol	SBA-0040-01
Triton™ X-100	Merck	Cat# 9036-19-5
Xylene	Carl Roth	Cat# CN80.1
Ethanol	Carl Roth	Cat# 5054.1
Antigen Retrieval Buffer (100X Tris-EDTA Buffer, pH 9.0)	abcam	Cat# ab93684
Zellkraftwerk Wash Buffer	Canopy Biosciences	Cat# 28050606/07-004
Zellkraftwerk Storage Buffer	Canopy Biosciences	Cat# 28050606/07-005
Critical commercial assays		
Click-iT EdU flow Cytometry Assay kit (Alexa Fluor 647)	Invitrogen,	Cat# C10424
IC Fixation/Permeabilzation Kit	eBioscience,	Cat# 88-8824-00
QuickExtractTM DNA Extraction Solution	Lucigen	Cat# QE0905T
GeneJet Gel Extraction Kit	ThermoFisher	Cat# K0692
GeneJet plasmid mini prep kit	ThermoFischer	Cat# K0503
Q5 High-Fidelity PCR Kit	New England Biolabs	Cat# M0491L
Mix2Seq genomics kit	Eurofins	N/A

(Continued on next page)

Continued

REAGENT or RESOURCE	SOURCE	IDENTIFIER
RevertAid first strand cDNA synthesis kit	ThermoFischer	Cat# K1622
RNeasy Mini Kit	Qiagen	Cat# 74106
Zymo Pure II Plasmid Maxiprep Kit	Zymo Research	Cat# D4202
Zombie UV™ Dye	Biolegend	Cat# 77474
CellXVivo Mouse Th17 Cell Differentiation Kit	R&D	Cat# CDK017
H&E Staining Kit (Hematoxylin and Eosin)	abcam	Cat# ab245880
Pan T cell Isolation Kit II, mouse	Miltenyi	Cat# 130-095-130
CD4$^+$ T cell Isolation Kit, mouse	Miltenyi	Cat# 130-104-454
μ-Dish 35 mm, high	ibidi	Cat# 81156
Double edge blades	EMS	Cat# 72000
PE/R-Phycoerythrin Conjugation Kit – Lightning-Link ®	abcam	Cat# ab102918
ZellSafe™ FFPE Tissue	Canopy Biosciences	Cat# 28050606/04
Calibration Slide for ZellScannerONE	Canopy Biosciences	Cat# 28050606/10-004
ZellSafe™ Box for storage of ZellSafe™ chips	Canopy Biosciences	Cat# 28050606/10-002
Zellsafe™ Washing Station	Canopy Biosciences	Cat# 28050606/10-001
Deposited data		
RNA-Seq mapping for breast 4T1 cells	This paper	http://genomics-lab.fleming.gr/cgi-bin/hgTracks?db=mm10&lastVirtModeType=default&lastVirtModeExtraState=&virtModeType=default&virtMode=0&nonVirtPosition=&position=chr12%3A76716084%2D76735713&hgsid=14120_VgLoy9452TmgOW9lyrewimpCkvLP
GEO mRNA sequencing dataset	https://www.ncbi.nlm.nih.gov/geo/query/acc.cgi	GSE202314
Raw data, code, and results of clustering analysis	This paper	https://github.com/Daria-Br/TCGA_clustering
Experimental models: Cell lines		
Mouse: 4T1	Wartenberg M., Jena, Germany	N/A
Mouse: 4T1-eGFP (PL-SIN-EF1α-EGFP)	This paper	N/A
Mouse: 4T1 Crispr mock	This paper	N/A
Mouse: 4T1 *Il22ra1*$^{-/-}$ KO	This paper	N/A
Mouse: 4T1 mock (pMCSV-Neo)	This paper	N/A
Mouse: 4T1 *Il22ra2*$^{+/+}$ (pMCSV-Neo-*Il22ra2*)	This paper	N/A
Mouse: 4T1 Crispr mock	This paper	N/A
Mouse: 4T1 *Pvr*$^{-/-}$	This paper	N/A
Mouse: 4T1 control (pMP71-Cerulean)		N/A
Mouse: 4T1 *Pvr*$^{+/+}$ (pMP71-*Pvr*-K2A-H2B-Cerulean)		N/A
Mouse: Line-1	Egilmez N.K., Louisville, KY, USA	N/A
Mouse: Line-1 mock (pMCSV-Neo)	This paper	N/A
Mouse: Line-1 *Il22ra2*$^{+/+}$ (pMCSV-Neo-*Il22ra2*)	This paper	N/A
Mouse: Line-1 Crispr mock (clone#1, #2, #3)	This paper	N/A
Mouse: Line-1 *Il22ra1*$^{-/-}$ KO (clone#4, #5, #6)	This paper	N/A
Mouse: Line-1 Crispr mock	This paper	N/A
Mouse: Line-1 *Pvr*$^{-/-}$	This paper	N/A
Mouse: Line-1 control (pMP71-Cerulean)		N/A

Continued

REAGENT or RESOURCE	SOURCE	IDENTIFIER
Mouse: Line-1 *Pvr*$^{+/+}$ (pMP71-*Pvr*-K2A-H2B-Cerulean)	This paper	N/A
Mouse: E0771	CH3 Biolabs	Cat# 940001
Mouse: E0771-eGFP (PL-SIN-EF1α-EGFP)	This paper	N/A
Human: Platinum-E (Plat-E) Retroviral Packaging Cell Line	Cell Biolabs	Cat# RV-101
Human: HEK293T	ATCC	Cat# CRL-3216
Experimental models: Organisms/strains		
Mouse: C57BL/6JRj	Janvier	SC-BALBJ-F
Mouse: C57BL/6NCrl	Charles River	632C57bl/6J
Mouse: BALB/cAnNCrl	Charles River	627Balb/cByJ
Mouse: C.129S5-*Il22*$^{tm1.1lex}$/Mmucd (*Il22*$^{-/-}$)	MMRRC, Lexicon Genetics	Stock number: 032402-UCD RRID: MMRRC_032402-UCD
Mouse: B6.C-Tg(CMV^{cre})1Cgn/J	Jackson Laboratory	Stock number: 006,054 RRID: IMSR JAX:006,054
Mouse: B6.Cg-Tg(*Cd4*^{cre})1Cwi/BfluJ	IMI, Munich	MGI:2386448
Mouse: B6;129S5-Il22tm1.1Lex/Mmucd (*Il22*^{flox})	MMRRC, Lexicon Genetics	Stock number: 036745-UCD Citation ID: RRID: MMRRC_036745-UCD
Mouse: B6-*Foxp3*^{mRFP} *Il17a*^{GFP} *Il22*^{BFP} (IL-22 BFP)	R. Flavell, Yale University, USA[19]	N/A
Mouse: B6.129S7-*Rag1*^{tm1Mom}/J (*Rag1*$^{-/-}$)	R. Flavell Lab, Yale University, USA	JAX:002,216 RRID: MGI:3582299
Oligonucleotides		
See Table S1 for Primer Sequences.		N/A
Recombinant DNA		
Plasmid: pMCSV-Neo	Takara (Clontech)	Cat# 634401
Plasmid: pMCSV-Neo-*Il22ra2*	This paper	N/A
Plasmid: PL-SIN-EF1α-EGFP	Addgene[96]	RRID: Addgene_21320
cDNA: murine *Il22ra2* mRNA sequence	This paper, from murine splenocytes	mRNA code: ENSMUST00000036564
Plasmid: pSpCas9(BB)-2A-GFP (PX458)	Addgene[97]	RRID:Addgene_48138
Plasmid: eSpCas9(1.1)	Addgene[98]	RRID:Addgene_71814
Plasmid: eSpCas(1.1)-2A-eGFP-*Il22ra1* CRISPR gene editing	This paper	N/A
Plasmid: eSpCas(1.1)-2A-eGFP-*Pvr* CRISPR gene editing	This Paper	N/A
Plasmid: pCMV-VSV-G	Addgene[99]	RRID: Addgene_8454
Plasmid: pCMV-dR8.2 dvpr	Addgene[99]	RRID: Addgene_8455
Plasmid: pMP71-K2A-H2B-Cerulean	C. Baum, Hannover, Germany	N/A
Plasmid: pMP71-*Pvr*-K2A-H2B-Cerulean	This paper	N/A
Software and algorithms		
Adobe Creative Suite CS6	Adobe	www.adobe.com/de/Creative_Cloud
GraphPad Prism 8.0	GraphPad	https://www.graphpad.com/
Microsoft Office 2019	Microsoft	https://products.office.com
Flowjo 10	Tree Star, BD	https://www.flowjo.com/
BD FACSDiva	BD Biosciences	https://www.bdbiosciences.com/en-in
Image Lab 5.2	BioRad	https://www.bio-rad.com/

(Continued on next page)

Continued

REAGENT or RESOURCE	SOURCE	IDENTIFIER
Living Image Software 4.7.2	Perkin Elmer	https://perkinelmer.com/Product/li-software-for-lumina-1-seat-add-on-128110
Imaris 7.2.3	Oxford instruments	https://imaris.oxinst.com/packages
Leica Application Suite X (LAS X)	Leica	https://www.leica-microsystems.com/
ZEN 2.3	ZEISS	https://www.zeiss.com/microscopy/en/products/software/zeiss-zen.html
Chop-Chop tool (sgRNA designer)	Labun et al.[100]	https://chopchop.cbu.uib.no/about
The Cancer Genome Atlas (TCGA)	National Cancer Institute	https://www.cancer.gov/tcga
Jupyter IDE 1.0.0	Project Jupyter	https://jupyter.org/
iPython 7.16.1	Perez and Granger[101]	https://ipython.org/
Jupyter Notebook 6.0.3	Kluyver et al.[102]	https://jupyter.org/
NumPy 1.22.3	Harris et al.[103]	https://numpy.org/
Pandas 1.4.2	Reback et al.[104] and McKinneyy W.[105]	https://pandas.pydata.org/
TensorFlow	Developers T.F.[106]	https://www.tensorflow.org/
Scikit-learn 0.23.1	Pedregosa et al.[107]	https://scikit-learn.org/
Matplotlib 3.5.1	Hunter J.D.[108]	https://matplotlib.org/
Seaborn 0.11.2	Waskom M.[109]	https://seaborn.pydata.org/
SciPy 1.8.0	Virtanen et al.[110]	https://scipy.org/
Lifelines 0.27.0	Davidson-Pilon C.[111]	https://lifelines.readthedocs.io/en/latest/
Openpyxl 3.0.9	Gazoni and Clark[112]	https://openpyxl.readthedocs.io/en/stable/
FCSwrite	Zellmechanik Dresden	https://github.com/ZELLMECHANIK-DRESDEN/fcswrite
ImageJ 1.52.	ImageJ	https://imagej.nih.gov/ij/
Fiji	Schindelin et al.[113]	https://github.com/fiji/fiji
Automatic image processing	Jarosch et al.[114]	https://github.com/SebastianJarosch/ChipCytometry-Image-Processing
Grid/collection stitching plugin	Preibisch et al.[115]	https://github.com/fiji/Stitching
BaSiC	Peng et al.[116]	https://github.com/marrlab/BaSiC
StarDist	Schmidt et al.[117]	https://qupath.readthedocs.io/en/stable/docs/advanced/stardist.html
ZellExplorer version 19-08-2020	Canopy Biosciences	N/A
ZellScan App version 2.21.21-1320	Canopy Biosciences	N/A
Pump control app [V1.0.0.5]	Canopy Biosciences	N/A
See Table S1 for Universal ProbeLibrary	Sigma-Aldrich	N/A

RESOURCE AVAILABILITY

Lead contact
Further information and requests for resources and reagents should be directed to and will be fulfilled by the lead contact, Sebastian Kobold (sebastian.kobold@med.uni-muenchen.de).

Materials availability
Materials generated in this study are available upon request to the lead contact, Sebastian Kobold (sebastian.kobold@med.uni-muenchen.de), pending the execution of an institutional material transfer agreement.

Data and code availability
The published article includes TCGA datasets analyzed during this study. The code and datasets generated during this study related to clustering analysis are available at the GitHub repository https://github.com/Daria-Br/TCGA_clustering. The RNA sequencing data are available in the Gene Expression Omnibus database (https://www.ncbi.nlm.nih.gov/geo/) under accession number GSE202314.

EXPERIMENTAL MODEL AND SUBJECT DETAILS

Mice

All animal experiments were approved by the local regulatory agencies (*Regierung von Oberbayern, Behörde für Soziales, Familie, Gesundheit und Verbraucherschutz*) and adhered to the European guidelines for the care and use of laboratory animals. Four to eight-week-old female mice were used for the experiments. Mice were used on Balb/c or C57BL/6 backgrounds where specified. For mouse line source and identification see the key resources table. Wild-type Balb/c mice were purchased from Janvier, and wild-type C57BL/6 mice were purchased from Janvier or Charles River. C.129S5-$Il22^{tm1.1Lex}$/Mmucd ($Il22^{-/-}$) and B6; 129S5-$Il22^{tm1.1Lex}$/Mmucd ($Il22^{flox}$) were obtained from the Mutant Mouse Resource and Research Center (MMRRC) at University of California at Davis, an NIH-funded strain repository, and was donated to the MMRRC by Genentech, Inc.[118] $Il22^{flox}$ mice were back-crossed for at least eight generations to a C57BL/6 background and were bred to CMV^{cre} or $Cd4^{cre}$ mice to generate $Il22^{-/-}$ and $Cd4^{cre}$; $Il22^{flox}$ lines. $Foxp3^{mRFP}$; $Il17a^{GFP}$; $Il22^{sgBFP}$ mice are the property of Richard A. Flavell.[19,119,120] $Rag1^{-/-}$ mice were purchased from Jackson Laboratories. Animals used in this study were maintained in individually ventilated cages under specific pathogen-free conditions at Klinikum der Universität München and University Medical Center Hamburg-Eppendorf.

Cell lines

The murine lung cancer cell line 1 (Line-1) was kindly provided by Nejat K. Egilmez (University of Louisville, KY). The 4T1 murine breast cancer cell line was kindly provided by Maria Wartenberg (Jena University Hospital, Jena, Germany). Line-1, 4T1, and E0771 cell lines (CH3 BioSystems) and their derivatives were cultured in RPMI 1640 (Sigma-Aldrich) supplemented with 10% FBS (Gibco), 100 μg/mL streptomycin, 1 IU/mL penicillin, and 2 mM L-glutamine (all PAA Laboratories). Cells were maintained at 37°C, with 5% CO_2. The Platinum-E (PLAT-E) retroviral packaging cell line (Cell Biolabs) was cultured in supplemented DMEM (Sigma-Aldrich), additionally containing 1 μg/mL puromycin and 10 μg/mL blasticidin (all from InvivoGen).

Mouse tumor models

For subcutaneous tumor implantation, 1.25×10^5 4T1 or 5×10^5 Line-1 cells in 100 μL PBS were injected s.c. into the right flank of BALB/c mice. Transgenic cell lines were prepared and injected at the same concentration as their respective parental cell line. Mouse health, weight, and tumor size were monitored every other day, as per local regulations. Tumor size was measured using a caliper and defined as an area (mm^2). Tumor sizes larger than 225 mm^2 or ulceration of the tumor were used as surrogate parameters for termination. For the intravenous metastatic model, 1.25×10^5 4T1 or 2×10^5 Line-1 cells in 100 μL PBS were injected in the lateral tail vein of Balb/c, or 0.5×10^6 E0771 cells in C57BL/6 mice. Mouse health and weight were monitored every other day. Typically, experiments were terminated 20 days after injection, unless otherwise indicated. Lungs were obtained and treated as described in *ex vivo* methods.

Intrasplenic (i.s.) tumor cell injection

For induction of forced liver metastases, mice received 250 μL PBS containing 3×10^5 cancer cells i.s. The injection was performed in hemi-spleen which was removed 3 min after the cancer cell injection. The mice were sacrificed after 3 weeks. Macroscopic metastases in livers were counted by using a stereoscope (Olympus Corporation, Germany).[121,122]

Adoptive T cell transfer

Total CD4$^+$ T cells were isolated from the spleen and lymph nodes using magnetic-activated cell sorting (MACS, Miltenyi Biotec) according to the manufacturer's instructions. $Rag1^{-/-}$; $Il22^{-/-}$ mice were engrafted with two million CD4$^+$ T cells from *WT* or $Il22^{-/-}$ mice, and injected intraperitoneally, for 4–5 weeks.

Quantification of macrometastasis and single-cell isolation from the lung

Mice were anesthetized with isoflurane and sacrificed by cervical dislocation. Lungs were perfused with ice-cold PBS to remove the excess blood and placed in cold complete RPMI until further processing. Macroscopic metastases were counted using magnification glasses. Lungs were cut into pieces <1 mm and incubated in collagenase (1 mg/mL) and DNase I (0.05 mg/mL, all Sigma-Aldrich) at 37°C for 30 min. Digested organs were passed through a 100 and 30 μM strainer and the single-cell suspension was washed with PBS. The remaining red blood cells were removed using Erythrocyte-lysis buffer (BD Pharm) for 3 min at room temperature (RT). The resulting lung single-cell suspension was used for flow cytometry (FC).

Lungs from the IL-22-BFP reporter animals were minced and incubated with collagenase (1 mg/mL) and DNase I (10 U/ml) at 37°C for 25 min on a shaking incubator in HBSS (with Ca^{2+} and Mg^{2+}). After washing with 1% FBS/PBS (v/v), cells were further separated using Percoll (GE Healthcare) gradient (67/40%, v/v) centrifugation. After centrifugation (400 g, 20 min, no brake) the interphase was collected, and the resulting single-cell suspension was used for flow cytometry.

Clonogenic metastasis assay

Single-cell suspension from the lung that contained tumor cells was diluted 1:10, 1:100, or 1:1000 in 10 mL of complete RPMI supplemented with 30 μM 6-thioguanine to inhibit non-tumor cell proliferation. Three technical replicates were plated for each sample in the 6-well plate. After 10 to 14 days, colonies that resulted from tumor cell proliferation were fixed with 70% ethanol (v/v) and stained

with a 1% (w/v) solution of crystal violet (all Sigma-Aldrich). The total number of colonies was counted and normalized to the mean of the control group.[123]

In vivo imaging
For *in vivo* imaging of tumor burden, mice were injected with 150 mg Luciferin per kg body weight 10 min before imaging according to the manufacturer's instructions (Xenolight D-Luciferin potassium salt) using IVIS Lumina X5. Analyses were performed with the Living Image Software 4.7.2 (all Perkin Elmer, USA).

METHOD DETAILS

Generation of 4T1-GFP and E0771-GFP cell lines
For the generation of the 4T1-GFP and E0771-GFP cell lines, the lentiviral vector PL-SIN-EF1α-eGFP was provided by James Ellis (#21320, Addgene). 8×10^6 HEK293T cells (ATCC) were seeded into a 10 cm, poly-L-Lysin-coated cell culture dish and cultured in complete DMEM for 12 h. The cells were then transfected with the lentiviral packaging vectors and the PL-SIN-EF1α-eGFP target vector. Five μg of VSV-G, 7.5 μg of pCMV, and 11 μg of the target vector were mixed and brought to a total volume of 500 μL with OptiMEM. The mixture was incubated at room temperature for 5 min and then mixed with 500 μL OptiMEM and 55 μL Lipofectamine 2000. The transfection mix was again incubated for 30 min at RT. HEK293T cells were then cultured in 1 mL of the transfection mix at standard culturing conditions. After 12 h, the medium was removed and switched to complete DMEM supplemented with 30% FBS. The virus supernatant was harvested after 24 to 48 h and passed through a 0.45 μm filter. HEPES Buffer (1:50) and polybrene (1:1000, Sigma-Aldrich) were added to the filtered virus supernatant. To proceed with the transduction, 5×10^5 4T1 or E0771 cells were plated in a 6-well plate. Four hours after seeding, the cell culture medium was removed, and 1 mL of the freshly acquired virus supernatant was added. After at least 4 h of incubation, 2 mL of fresh culture medium was added. Forty-eight hours post-transduction, GFP-positive cells were sorted using a BD FACS Aria III to obtain purities of GFP$^+$ 4T1 or E0771 cells >95%.

Generation of IL-22BP-producing (*Il22ra2*$^+$) cells
Murine *Il22ra2* (IL-22-BP) cDNA was purchased from GeneScript. DNA insert was cloned into the retroviral pMSCV-Neo plasmid (Clontech) following standard molecular cloning protocols.[124] Constructs were verified by Sanger sequencing using the Mix2Seq kit (Eurofins) according to the manufacturer's instructions. The validated plasmid was expanded in competent *E. coli* DH5α (NEB) and purified using Zymo Pure II Plasmid Maxiprep Kit (Zymo Research). For retroviral expression, pMCSVn-Neo and pMCSVn-Neo-*Il22ra2* plasmids were transfected into the PLAT-E cell line (Platinum-E retroviral packaging cell line, Cell Biolabs) using Lipofectamine 2000 transfection as described. After 48 h supernatant containing viral particles was collected and filtered using a 0.45 μm filter. Two mL of fresh viral supernatant that contained 8 μg/mL polybrene (Sigma-Aldrich) was added to 4T1 or Line-1 target cells followed by centrifugation at 800 *g* for 30 min at 32°C and incubated for 24 h. Then the medium was exchanged to RPMI and incubated for an additional 24 h for a total of 48 h. Transduced cells were selected with the addition of 800 μg/mL of Geneticin G418 (Thermofisher) for two weeks.

Generation of *Il22ra1*$^-$ and *Pvr*$^-$ cell lines using CRISPR/Cas9 system
The CRISPR/Cas9 system was employed to generate *Il22ra1*$^-$ and *Pvr*$^-$ cell lines, respectively. sgRNAs were designed using the on-line tool CHOPCHOP (*Il22ra1*-sgRNA: cta ctg acc atc ctg acg gt, *Pvr*-sgRNA: ggc caa gag att cgt cca gg) and subsequently cloned via *Bbs*I into the eSpCas(1.1)-2A-eGFP plasmid, which was generated by introducing the T2A-eGFP fragment from PX458 into eSp-Cas9(1.1) via *Fse*I and *Not*I.[100,98] Individual plasmids were a gift from Feng Zhang (Addgene plasmids #71814 and #48138). 4T1 and Line-1 cells were plated in 6-well plates and transfected using a mix containing 250 μL of Opti-MEM (Sigma-Aldrich), 5 μg of the respective plasmid, and 12 μL Lipofectamine 2000 (Thermofisher) for 18 h, followed by regular culture medium for another 24 h. Afterward, *Il22ra1*-edited cells were sorted with a BD FACSAria III and single-cell clones were grown in 96-well plates. Clones were analyzed by Sanger sequencing using QuickExtract DNA Extraction Solution (Lucigen) and Mix2Seq Kit (Eurofins) according to manufacturers' instructions. *Il22ra1*$^-$ clones were further validated by the absence of IL-22 induced Stat3 phosphorylation using Western blot (data not shown), clones that failed to show diminished Stat3 phosphorylation were selected as controls. *Pvr*-edited cells were stained with an anti-mouse CD155-PE Antibody (BioLegend) and enriched by FACS at a purity of >95%. CD155-PE$^-$ (*Pvr*$^-$) and CD155-PE$^+$ (control) cells were then used in subsequent experiments.

Next-generation sequencing
0.3×10^5 4T1 cells were seeded into six-well plates and incubated in complete RPMI media for 24 h. Cells were then washed twice with PBS, and 1 mL of Opti-MEM serum-free medium with or without 100 ng/mL of IL-22 was added to each of the three biological replicates. Cells were incubated for 24 h and proceeded to RNA extraction by the TRIzol method following the manufacturer's instructions (Invitrogen).

Total RNA was measured in NanoDrop (ND1000 Spectrophotometer, PEQLAB). Samples were diluted to a mean concentration of approximately 100-150 ng/μL and their quality was assessed in a Bioanalyzer (Agilent Technologies) using the Agilent RNA 6000 Nano Kit reagents and protocol (Agilent Technologies). For library preparation, the 3′ mRNA-Seq Library Prep Kit protocol for Ion Torrent (QuantSeq-LEXOGEN Vienna, Austria) was used according to the manufacturer's instructions. Up to 500 ng of RNA was

used for first and second-strand synthesis, followed by 13 cycles of amplification. Library quality and quantity were assessed in Bioanalyzer using the DNA High Sensitivity Kit reagents and protocol (Agilent Technologies). The quantified, barcoded libraries were pooled together at a final concentration of 7 p.m. The pools were templated and enriched on an Ion Proton One Touch system. Templating was performed using the Ion PI Hi-Q OT-II 200 Kit (ThermoFisher Scientific), followed by sequencing with the Ion PI Hi-Q Sequencing 200 Kit on Ion Proton PI V2 chips (ThermoFisher Scientific) according to commercially available protocols, on an Ion Proton System, according to the manufacturer's instructions.

Short read mapping
The obtained FASTQ files were mapped on the UCSC hg19 reference genome using a two-phase mapping procedure. Firstly, the short reads were mapped using tophat2, with default settings, and using additional transcript annotation data for the hg19 genome from Illumina iGenomes (http://cufflinks.cbcb.umd.edu/igenomes.html). Next, the reads which remained unmapped were submitted to the second round of mapping using Bowtie2 with the –local and –very-sensitive local switches turned on.

Differential expression analysis
Differential expression analysis was performed using the Bioconductor package metaseqR (https://www.ncbi.nlm.nih.gov/pubmed/25452340). The BAM files obtained after short-read mapping, one for each RNA-Seq sample, were summarized in a 3'UTR read counts table, using the Bioconductor package GenomicRanges. In the final read counts table, each row represented a gene, each column one RNA-Seq sample, and in each cell, the corresponding read counts were associated with each row and column. The gene counts table was normalized for inherent systematic or experimental biases (e.g., sequencing depth, gene length, GC content bias, etc.) using the Bioconductor package DE-Seq after removing genes that had zero counts over all the RNA-Seq samples. Before the statistical testing procedure, the gene read counts were filtered for possible artifacts that could affect the subsequent statistical testing procedures. Genes presenting any of the following were excluded from further analysis: i) genes with a total length less than 500, ii) genes whose average reads per 100 bp was less than the 25 th quantile of the total normalized distribution of average reads per 100 bp, iii) genes with read counts below the median read counts of the total normalized count distribution, iv) genes whose Ensembl biotype matched the following: rRNA, TR_V_pseudogene, TR_J_pseudogene, IG_C_pseudogene, IG_J_pseudogene, IG_V_pseudogene, v) genes where 50% of samples did not present more than five normalized counts across all samples. The resulting gene counts table was subjected to differential expression analysis for the contrasts WM versus Ctrl using a combination of the Bioconductor packages DE-Seq, edgeR, limma, NBPSeq, and NOISeq. To combine the statistical significance from the multiple algorithms, the PANDORA weighted p value across the results method was calculated and applied.

RNA isolation and RT-qPCR
Total RNA from tumor cell lines was isolated using the RNeasy Mini Kit (Qiagen) according to the manufacturer's instructions. The RNA concentration was determined with Nanodrop 2000c (Thermofisher). cDNA was synthesized using the RevertAid first-strand cDNA synthesis kit (Thermofisher). Relative mRNA expression was determined by real-time-qPCR. Kapa Probe Universal Master Mix (Roche) and specific probes were by Roche, and primers are from Metabion (see Table S1). Sample cDNA was amplified and measured by LightCycler 480 (Roche). Expression fold change was calculated using the $\Delta\Delta Ct$ method.

Flow cytometry
For the detection of 4T1-GFP and E0771-GFP cells, single cells from the lungs were stained with Fixable Viability Dye, eFluor 780 (Thermofisher) according to manufacturer's instructions, resuspended in 400 μL FC buffer (1% FBS/PBS) and measured by LSR Fortessa II (BD) using appropriate controls. Absolute numbers of cells were determined using CountBright beads (Thermofisher) according to the manufacturer's instructions.

For the intracellular detection of IL-22 production, single cells from the lungs of control and tumor-injected mice were incubated for 4 h at 37°C in complete RPMI containing 50 ng/mL PMA, 1 μg/mL Ionomycin, 1 μL/mL of GolgiPlug (BD), 0.7 μL/mL GolgiStop (BD), 1 μL/mL 2-Mercaptoethanol.[125] After incubation, cells were washed with PBS and incubated with TruStain FcX (Biolegend) in FC buffer for 15 min at 4°C followed by washing with FC buffer and staining with antibodies for extracellular antigens and viability dye for 20 min at 4°C according to the Key resources table. Then, cells were washed with FC buffer, fixed and permeabilized by Cytofix/Cytoperm Kit (BD) following manufacturer's instructions and incubated with intracellular antibody in Wash buffer (BD) for 30 min at 4°C, washed by Wash (BD) buffer, resuspended in 400 μL FC buffer and analyzed by LSRFortessa II (BD). Data were analyzed with FlowJo software (Flowjo LLC, BD).

Generation of Th17 cells from mouse splenocytes
Mouse T cells were isolated from solenocyte cell suspension using pan T cell isolation kit II (Miltenyi). Cells were cultured under polarizing conditions using CellXVivo mouse Th17 cell differentiation kit (R&D) according to the manufacturer's instructions for 5 days and then analyzed by flow cytometry.

Proliferation assessment using EdU
For early metastasis assay, 5 x 10^{6} 4T1-GFP cells were prepared, resuspended in 100 μL PBS and injected into the lateral tail vein of WT BALB/c or IL22 KO mice. Mice were sacrificed 12 or 48 h after injection. Four hours before termination, mice were injected

intraperitoneal with 100 mg/kg of 5-ethynyl-2-deoxyuridine (EdU), a thymidine analog that is incorporated by the proliferating cells. The cell suspension was prepared from the left lung and stained before measurement with Click-iT EdU Flow Cytometry Kit according to the manufacturer's instructions. The right lung lobule was preserved fresh at 4°C in PBS on ice and analyzed using the confocal microscope.

Confocal microscopy

Fresh lung lobules were submerged in a PBS solution containing 5 μg/mL of Hoechst 33,342 for 10 min at room temperature. Subsequently, the tissue was carefully flattened with a glass cover slide and directly exposed to the Leica TCS SP5 confocal system. Two hundred pictures representing an area of 25 mm^2 were acquired per sample. Quantification of total GFP$^+$ cells was performed by ImageJ and normalized by mm^2 of the tissue.

iDISCO tissue clearing and light-sheet microscopy

Freshly perfused right lung lobes were placed in 4% PFA overnight at 4°C with rocking. Samples were stained and cleared following the modified iDISCO protocol.[52] For this, samples were washed twice in PBS for 1 h, then placed in 50% methanol in PBS for 1 h, followed by 80% methanol for 1 h, then 100% methanol for 1 h twice. Samples were then bleached with 5% hydrogen peroxide in 20% DMSO-methanol (1 vol 30% H$_2$O$_2$: 1 vol DMSO: 4 vol methanol, ice-cold) at 4°C overnight. After bleaching, samples were washed in methanol for 1 h twice, then in 20% DMSO-methanol for 1 h twice followed by 80% methanol for 1 h, 50% methanol for 1 h, PBS for 1 h twice, and finally in 0.2% Triton X-100 in PBS for 1 h twice before further staining procedures. Pretreated samples were incubated in a solution containing 0.2% Triton X-100, 20% DMSO, 0.3 M glycine in PBS at 37°C overnight and then blocked in a solution containing 0.2% Triton X-100, 10% DMSO, 6% Donkey Serum at 37°C for 1 day to prevent unspecific binding. Samples were washed twice with PTwH solution (0.2% Tween 20 in PBS supplemented with 10 μg/mL heparin) for 1 h and then incubated in GFP-Booster (Chromotek - gba488-10) dilutions in PTwH solution with 5% DMSO and 3% Donkey Serum at 37°C for 4 days with rotations. Samples were finally washed in PTwH for 2 days before clearing and imaging. Samples were incubated overnight in 10 mL of 50% (v/v) tetrahydrofuran in H$_2$O (THF, Sigma 186,562-12X100ML). Samples were then incubated for 1 h in 10 mL of 80% THF in H$_2$O, twice for 1 h in 100% THF, and then in dichloromethane (DCM, Sigma 270,997-12X100ML) until they sank to the bottom of the vial. Finally, samples were incubated in 18 mL of dibenzyl ether (DBE, Sigma 108,014-1KG) until transparent (~2 h) and then stored in DBE at RT. Samples were imaged in DBE by a light-sheet fluorescence Ultra-Microscope II (LaVision).

Precision-cut lung slices (PCLS) and confocal microscopy

Lung tissue samples from *Foxp3*^{mRFP}; *Il17a*^{GFP}; *Il22*^{sgBFP} mice, that were injected intravenously with 2 x 10^5 E0771 tumor cells in 100 μL of PBS, were used to generate PCLS.[126] Lungs were perfused with cold PBS containing 5 IU/mL heparin. Approximately 1.0 mL of 2% low melting point agarose (Biozym) at 40°C was slowly injected through the tracheal incision using a 20 G vein catheter. After 5 min of solidification at 4°C, the lung lobules were excised and submerged into ice-cold PBS. Subsequently 250 μm thick slices were prepared using the Leica VT1200 S vibratome. The staining procedure consisted of incubating the samples overnight with anti-mouse CD4 antibody at a concentration of 10 μg/mL and with PE anti-mouse CD155 antibody (both from Biolegend) at a concentration of 10 μg/ml. Nuclear staining followed the day after using NucRed Live 647 ReadyProbes reagent containing TO-PRO-3 DNA dye (Thermo Fisher) for 30 min, according to the manufacturer's protocol. After staining, the samples were washed six times in PBS.

The PCLS were embedded with antifade mountant Pro-Long Glass (Thermo Fischer) onto 35 mm imaging dishes (ibidi) according to the manufacturer's protocol. Confocal microscopy using the Zeiss LSM800 confocal system was performed acquiring 15 images of metastasis and normal tissue per sample representing an area of 160 x 160 μm^2. Metastatic tissue was identified according to its CD155 expression. Z-Stacks consisting of 20 images with a 1 μm interval were generated using sequential imaging mode. The ZEN 2.3 software (Zeiss), including 3D view (by Arrivis) and colocalization plug-ins, was used for quantification and analysis.

H&E staining

Murine lungs were formalin-fixed, followed by a dehydration step conducted with the Shandon Citadel 2000 Tissue Processor. Subsequently, the lungs have been embedded in paraffin blocks and cut into sections of 3 μm thickness onto microscopic slides. For visualization of metastases, the sections were then stained for hematoxylin and eosin (H&E Staining Kit by abcam). For that, a rehydration step with a series of xylol (I), xylol (II) (each for 2 min), 100%, 96%, and 70% ethanol (for 1 min) has been performed. Samples were briefly rinsed with cold water (30 s), stained with hematoxylin for 6 min, rinsed with warm water for 4 min and with 70% ethanol for 1 min, stained with eosin for 2.5 min and dehydrated with series of 96% (I), 96% (II), 96% (III), and 100% ethanol (each 1 min). Lastly, the slides were put into xylol (2.5 min). After drying overnight at room temperature protected from sunlight, the samples were digitalized with the EVOS M7000 Imaging System (Thermo Fisher Scientific).

Chip cytometry

For chip cytometry, paraffin blocks were then cut into 3 μm thick sections with a semi-automatic microtome (Fisher Scientific), mounted on Zellkraftwerk FFPE Coverslips (Canopy), and left to dry overnight at 40°C in a dry atmosphere. Deparaffination of the samples was achieved by incubating the sections at 60°C for 1 h in a dry atmosphere, followed by two incubations in Xylol (Carl Roth) for 2 min each. Then, the samples were rehydrated in a descending ethanol row as described previously, followed by a

wash in PBS for 5 min. After that, antigen retrieval was performed for 20 min at 95°C in antigen retrieval buffer (Tris-EDTA, pH 9, abcam), followed by 20 min of cooldown. After washing in PBS for 5 min, sections were permeabilized in 0.1% Triton X-100 (Merck) for 15 min and washed again in PBS. Sections were then mounted onto Zellsafe FFPE Tissue Chips (Canopy) which were subsequently loaded with ZKW storage buffer (Canopy) and stored at 4°C until use.

Images were acquired on the ZellscannerONE (Canopy) platform as described.[60,114] Background fluorescence of the tissues was acquired for each channel to be subtracted from the immunofluorescence signal in the subsequent imaging steps. The sections were blocked for unspecific binding in PBS, supplemented with 5% (v/v) donkey serum (Thermo Fisher) for 1 h at room temperature. The samples were incubated with a goat anti-murine NKp46 antibody (R&D) at a concentration of 5 μg/mL overnight at 4°C. The following day, FITC conjugated donkey anti-goat antibody (Jackson ImmunoResearch) was applied at a concentration of 10 μg/mL for 2 h at room temperature. After intensive washing with Zellkraftwerk washing buffer (Canopy), a fluorescence signal was acquired, followed by a step of photobleaching and an acquisition of background fluorescence for the following staining. Next, the sections were blocked in PBS containing 5% (v/v) rabbit serum for 1 h at room temperature. Rabbit anti-murine CD155 antibody (abcam) was conjugated with PE using the Lightning Link conjugation kit (abcam), following the manufacturer's instructions, before being used for staining at a concentration of 5 μg/mL overnight at 4°C. After a washing step, imaging and photobleaching were performed as described before. Following this, the tissue was incubated with rabbit anti-murine CD8 antibody (abcam), conjugated with AF555, at a concentration of 10 μg/mL overnight at 4°C, followed by washing and an imaging cycle the following day. Lastly, DNA was stained with 0.4 μM Hoechst 33,342 (Thermo Fisher) for 5 min followed by a washing step and imaging.

Chip cytometry image processing and segmentation

Chip cytometry samples were processed and segmented in ImageJ (Fiji distribution)[113] utilizing an established pipeline.[60] Briefly, 16bit grayscale TIFFs of net fluorescence signal for each marker were stitched with the grid-collection plugin available through Fiji[115] after shading correction with the BaSiC plugin.[116] Then a merged image with the pseudo coloring of each marker was generated. For quantification, the sections were segmented on the nuclear stain by a pre-trained neural network from StarDist. The resulting regions of interest (ROI) were enlarged by 1 μm and fluorescence values were calculated after image preprocessing.[60] The output.csv file was then formatted into a.fcs file containing mean fluorescence intensity, x and y coordinates, area, and circularity for each detected cell, with the python plugin FCSwrite (https://github.com/ZELLMECHANIK-DRESDEN/fcswrite) for further analysis in FlowJo.

Cells recognized by neural network segmentation as described above were gated on area and circularity. Then, each marker was plotted against an area to identify NK cells (NKp46⁺), CD8 T cells (CD8⁺), and tumor cells (CD155⁺). The density of CD155⁺ cells was used to gate on the metastatic lesion. The spatial gates generated in this step were then applied to the CD8 T and NK cells to quantify intralesional abundance thereof. Further, mean fluorescence values of CD155 were calculated for each metastatic lesion.

TCGA data analysis

We used Illumina HiSeq RNA sequencing data from The Cancer Genome Atlas (TCGA). For this study, we chose the TCGA Lung Adenocarcinoma (LUAD) and invasive breast carcinoma (BRCA) datasets. Gene expression data was acquired for *PVR*, *IL22RA1*, *IL22RA2*, and *IL10RB*. We chose not to include *IL22* gene expression as it was reported only for a fraction of the samples. Data for the sample type, pathologic stage (from TNM classification), overall survival events, and overall survival time comprised the main analyzed phenotypic features.

We used the University of California Santa Cruz's Xena Functional Genomics Browser (UCSC Xena) for browsing, pre-filtering, and acquisition of TCGA datasets. We chose JupyterLab (2.1.5, Python 3.9, Anaconda distribution) as our environment for data handling and analysis. Most data structuring and basic analyses were done with the Pandas library (1.0.5). We used methods from the Scikit Learn (0.23.1) and Scipy (1.5.0) libraries for scaling of data, t-distributed Stochastic Neighbor embedding (t-SNE) dimensionality reduction, and agglomerative clustering. Matplotlib (3.2.2) and Seaborn (0.10.1) libraries were used for plotting. The Lifelines (0.26.3) library was used for Kaplan Meyer plotting, Restricted mean survival time (RMST), and Cox's proportional hazards model analyses.

RNA-seq-by Expectation Maximization (RSEM) values were normalized as $\log_2(x+1)$ by UCSC Xena. We used UCSC Xena's filtering options to filter out patient samples with null values for any of the chosen parameters and downloaded the resulting tables, containing genomic and phenotypic data, for further processing and analysis. The datasets were filtered for primary tumor samples. We filtered the BRCA dataset for HER2-positive samples. Then, the gene expression data was scaled with a *Z* score for clustering and improved plotting.

We reduced the dimensionality of the gene expression data down to two dimensions by t-distributed stochastic neighbor embedding (t-SNE). We chose a perplexity value of 20, as values ranging from 5 to 50 have been reported to be robust.[127]

We used agglomerative clustering, a bottom-up method of hierarchical clustering, to stratify our dataset by gene expression patterns in an unsupervised way. We used Ward's minimum variance algorithm as our linkage method and Euclidean distance as our distance metric. This linkage hierarchy can be visualized with a dendrogram plot. Here, we observed that the dataset was separated into three main clusters, that were formed in most iterations of the algorithm. Based on this, we chose to fit three clusters to the datasets. The resulting labels were joined with the scaled, multidimensional datasets for further analyses.

We utilized Kaplan Meier (KM) Plots to analyze the impact of the gene expression patterns on the overall survival of the patients. Statistical significance was tested with the log rank test. To account for the high variance at later time points of the KM plots, we

performed Restricted Mean Survival Time (RMST) for the first five years of follow-up to quantify survival differences. RMST values of the patient clusters were subtracted from each other as a measure of relative survival time gain or loss in dependence on cluster affiliation. The Cox Proportional Hazards model (CPH) was used to quantify the impact of each gene on the survival phenotype.

We summarized the pathologic stages IA & IB to stage I, IIA & IIB to stage II, and IIIA & IIIB to stage III because only the non-detailed classification was available for most samples. The statistical significance of the frequency differences was determined by the chi-squared test.

Deconvolution analysis

To have a deeper insight into the different immune landscapes of the IL-22-PVR signature clusters, we used the Cell Fractions analysis module of CIBERSORT. This tool allows deconvolution of immune-cell subsets from bulk RNAseq samples, by fitting distinct, cell-type-specific gene expression patterns onto them, that are compiled in a signature matrix. Here, we used the LM22 signature matrix file, provided by CIBERSORTx, enabling the enumeration of 22 immune cell subtypes.[128]

We acquired gene expression data from the TCGA LUAD dataset for 509 of 547 genes of the LM22 signature matrix from UCSC Xena. $\log_2(x+1)$ normalized RSEM gene expression values from the TCGA LUAD cohort were brought out of the $\log_2$ space by inversion of the normalization, using Numpy operations. We further filtered the resulting table for patient samples that were assigned to an IL-22-PVR signature cluster, before formatting the resulting table for CIBERSORTx deconvolution. CIBERSORTx was run in absolute and relative mode with enabled B-mode batch correction, disabled quantile normalization, and 1000 permutations. We re-joined the resulting tables with IL-22-PVR signature cluster labels using the TCGA sample codes as unique identifiers.

QUANTIFICATION AND STATISTICAL ANALYSIS

The normality of the datasets was determined using the D'Agostino and Pearson test. Outliers were identified using the ROUT method, 1%. Differences between experimental conditions in normally distributed datasets were analyzed using the unpaired two-tailed Student's t test. Welch's correction was applied to the datasets with significant differences in SD Otherwise, the two-tailed Mann-Whitney nonparametric U test was used. P-values are indicated in each figure, $p < 0.05$ was considered significant. All statistical tests were performed using GraphPad Prism 8-10 (GraphPad software).